Research Square

Preprints are preliminary reports that have not undergone peer review.
They should not be considered conclusive, used to inform clinical practice,
or referenced by the media as validated information.

Mapping the fate of unstable manifolds departing from Earth-Moon Halo and Near Rectilinear Halo Orbits: a dynamical characterisation of low-energy transport in cislunar space

Mathilda Bolis

mathilda.bolis@polimi.it

Politecnico di Milano

Joan Pau Sánchez Cuartielles

Institut Supérieur de l'Aéronautique et de l'Espace (ISAE-SUPAERO)

Elisa Maria Alessi

National Research Council

Stéphanie Lizy-Destrez

Institut Supérieur de l'Aéronautique et de l'Espace (ISAE-SUPAERO)

Camilla Colombo

Politecnico di Milano

Research Article

Keywords:

Posted Date: November 20th, 2026

DOI: https://doi.org/10.21203/rs.3.rs-11652027/v1

License: This work is licensed under a Creative Commons Attribution 4.0 International License.
Read Full License

Additional Declarations: No competing interests reported.

Mapping the fate of unstable manifolds departing from Earth-Moon Halo and Near Rectilinear Halo Orbits: a dynamical characterisation of low-energy transport in cislunar space

Mathilda Bolis[1*], Joan Pau Sánchez Cuartielles[2†], Elisa Maria Alessi[3†], Stéphanie Lizy-Destrez[2†], Camilla Colombo[2†]

[1*]Dipartimento di Scienze e Tecnologie Aerospaziali, Politecnico di Milano, Via La Masa 34, Milano, 20156, Italy.
[2]Département Conception et Conduite des véhicules Aéronautiques et Spatiaux, Institut Supérieur de l'Aéronautique et de l'Espace, Avenue Marc Pélegrin 10, Toulouse, 31400, France.
[3]Istituto di Matematica Applicata e Tecnologie Informatiche "Enrico Magenes", Consiglio Nazionale delle Ricerche, Via Alfonso Corti 12, Milano, 20133, Italy.

*Corresponding author(s). E-mail(s): mathilda.bolis@polimi.it;
Contributing authors: joan-pau.sanchez@isae-supaero.fr; elisamaria.alessi@cnr.it; stephanie.lizy-destrez@isae-supaero.fr; camilla.colombo@polimi.it;
†These authors contributed equally to this work.

Abstract

As cislunar space becomes increasingly populated, ensuring safe operations in the Earth-Moon (EM) system is fundamental to mitigating the risk of generating space debris. In this paper, we propose a framework for investigating the evolution of low-energy trajectories associated with objects departing from EM Libration Point Orbits (LPOs) to design low-cost disposal options. Trajectories

lying on both the interior and exterior branches of the unstable manifolds of some selected LPOs are propagated for up to twelve months within the coupled Circular Restricted Three-Body Problem (CR3BP). Fate maps are constructed to describe the long-term evolution of these trajectories as a function of the departure phase angle along the LPO, $\boldsymbol{\theta_0}$, and the phase angle between the EM and SE systems, $\boldsymbol{\alpha_0}$. This allows identifying areas of the maps associated with transport to different regions of the Sun-Earth-Moon system or with Moon or Earth impacts. The observed behaviours are then compared across the different cases considered, enabling a global mapping of the problem, and analysed in relation to selected dynamical indicators. Investigating the links between these indicators and the patterns emerging in the maps provides a dynamical interpretation of low-energy transport and its relevance to end-of-life disposal design.

Keywords: Earth-Moon system, Disposal at End-of-Life, Space Traffic Management, Libration Point Orbits, Low-energy transport, Manifold dynamics, Coupled CR3BP, Fate maps

1 Introduction

In the coming years, space traffic is expected to increase, and to do so also towards the cislunar region, Baker-McEvilly et al. (2024), European Space Policy Institute (ESPI) (2025). Recently, interest in returning to the Moon has grown, driven by large-scale programs such as Artemis, while near-Earth space becomes increasingly congested, as the number of objects in orbit has steadily increased since the beginning of the space age. A significant fraction of these consists of uncontrolled space debris, including decommissioned satellites and fragments generated by surfaces' degradation, collisions, and explosions. While the need for space traffic management and space situational awareness infrastructures in near-Earth space is now more evident than ever, it is also important to prepare to solve the challenge of managing and preventing the debris problem in a region characterised by strong non-linear dynamics, such as the Earth-Moon (EM) system.

To this end, recent studies have focused, on modelling potential fragmentation events (e.g., Boone et al. (2025); Guardabasso et al. (2023); Black and Frueh (2025)),

collision avoidance manoeuvres (e.g., Bucchioni et al. (2022); Tu et al. (2025); Nugent et al. (2025)), and the development of cislunar space situational awareness infrastructures (e.g., Frueh et al. (2021); Gambarotto et al. (2026); Shimane et al. (2025)). However, to prevent the creation of space debris in the first place, it is necessary to develop a framework capable of readily identifying low-cost, safe, and robust End-of-Life (EoL) disposal solutions applicable to a wide range of mission scenarios. According to the ESA Space Debris Mitigation Working Group (2023) report, four main EoL disposal strategies can generally be applied to spacecraft in the EM system, "in order of preference: heliocentric disposal, lunar impact, Earth re-entry, or a lunar graveyard orbit". Heliocentric disposal was studied by Davis et al. (2019a), Davis et al. (2019b), Boudad et al. (2022), Scheuerle et al. (2023), Sargent et al. (2025) and Bolis et al. (2026a), particularly in relation to the 9:2 Near Rectilinear Halo Orbit (NRHO), which was selected as the reference orbit for the Lunar Gateway; and by Olikara et al. (2015), Armellin et al. (2015), Colombo et al. (2015) and Soldini et al. (2016) with reference to orbits in the Sun–Earth (SE) system. Furthermore, Bucci et al. (2018) studied the escape dynamics from periodic orbits in the Sun–Earth–Moon system, although he did not directly link this aspect to the disposal design. Other authors, Davis et al. (2019b), Andrievskaia et al. (2022), Guardabasso (2023), Boone and Bettinger (2025), Carton and Rosengren (2025), and Bolis et al. (2026a), investigated lunar impact disposal trajectories in the EM system. Conversely, Earth re-entry and graveyard-orbit disposal strategies have not yet been addressed systematically within the EM framework, with most of the existing literature focusing instead on the SE system, Alessi (2015). Overall, the graveyard orbit option remains the least explored, as it is often considered the least robust disposal strategy and the one associated with the highest operational costs. Indeed, disposal into a graveyard orbit would require a transfer from the mission's reference periodic orbit to a stable orbit or dynamical region of limited operational interest. Potential candidates include distant retrograde

orbits or orbits around the EM-L_4 and L_5 points. However, transferring to these locations may be particularly expensive in terms of ΔV, precisely because of their stable nature, or may imply local transfer opportunities. Furthermore, such a disposal strategy would require continuous monitoring from Earth or a space-based station and the capability to mitigate any eventual departure from the designated region.

The preliminary step to develop a comprehensive framework for identifying low-cost disposal solutions is to understand the dynamics governing first the EM (e.g. Bolis et al. (2026b)), and then the Sun-Earth-Moon system, with a focus on the mechanisms driving transport from Libration Point Orbits (LPOs) to other regions. Manifolds allow for the definition of low-energy transport and, consequently, of low-cost disposal trajectories (e.g. Olikara et al. (2015), Armellin et al. (2015), Colombo et al. (2015) and Soldini et al. (2016)). The starting point is the investigation of unstable manifold trajectories' evolution following departure from LPOs in the EM system. Another perspective of the same problem was extensively studied in the context of transfers from the Earth to the Moon (e.g. Belbruno and Miller (1993), Koon et al. (2001), Mingotti et al. (2009), Alessi et al. (2009), Alessi et al. (2010), Renk et al. (2010), Parker and Anderson (2014), Scheuerle et al. (2025), Zhang et al. (2025)). However, considerably less attention has been devoted to transfers in which the objective is not to reach an LPO but rather to depart from it and characterise the subsequent dynamical evolution of the resulting trajectory. When studied, the analysis of trajectories departing from the EM system along natural dynamical pathways found applications beyond disposal design, focusing instead on eventual transfers to other planets. To cite some examples, Richmond and Howell (2026) studied low-energy transfers from the Moon to Mars, Liu et al. (2026) studied escape from the EM Zero Velocity Surfaces (ZVSs) with departure from Earth and lunar gravity assists, and Pasquale et al. (2024) studied opportunities for the eventual exploitation

of escape trajectories from the EM system to reach the near-Earth asteroids region.

In this paper, we present a framework for the identification of low-energy trajectories departing from selected LPOs of the EM system: one NRHO and two Halo orbits associated with EM-L_1, together with their counterparts associated with EM-L_2. The natural evolution of their unstable manifolds within the coupled Circular Restricted Three-Body Problem (CR3BP) is mapped as a function of two parameters: the phase angle along the LPO associated with a given unstable manifold trajectory initial condition, θ_0, and the phase between the EM and SE systems at departure, α_0. In the coupled CR3BP framework, trajectories are propagated considering the EM CR3BP dynamics until the gravitational acceleration exerted by the Sun on a given trajectory becomes greater than that exerted by the Moon. At that point, the dynamical model is switched to SE CR3BP. The proposed global mapping approach leads to the development of fate maps that provide a preliminary identification of the transport classes associated with a given combination of initial conditions. The resulting trajectories are then further classified according to their dynamical characteristics and to the dominant influence exerted by the different bodies on their evolution. Subsequently, the maps are characterised to assess the respective roles of the Sun and the EM system in shaping the observed behaviours, for example, by analysing escape trajectories through the evolution of their eccentricity with respect to the Earth, etc., and a dynamical interpretation of the patterns visible in the maps is given. Finally, the results are related to the evolution of the Jacobi Constant (JC) and the Finite-Time Lyapunov Exponent (FTLE) of the trajectories, evaluated at different characteristic times, and the evolution of these quantities is compared with the fate maps. The objective is to establish a preliminary dynamical cartography of the natural pathways present in the EM system, their interactions, and the key dynamical parameters governing their evolution, with the ultimate aim of exploiting this knowledge in a subsequent phase of this work for

the systematic design of EoL disposal strategies, as already introduced, for instance, by Bolis et al. (2026c). The goal is to derive a comprehensive framework capable of encompassing a wide range of cases, both in terms of the reference LPOs from which trajectories depart and the initial departure conditions associated with natural transport pathways, namely unstable manifolds, together with a dynamical interpretation of the patterns observed. Beyond disposal applications, the proposed analysis may also be interpreted as a novel approach to transfer design, including transfers from the Earth to the Moon or from the Moon to other planets, and the identification of heteroclinic connections between different LPOs. The remainder of the paper is organised as follows. Sections 2 and 3 introduce the CR3BP and the coupled CR3BP frameworks, while Section 4 describes the transformation between the EM rotating and Earth-centred J2000 reference frames. Section 5 presents the LPOs selected for the analysis, and Section 6 discusses the behaviour of their unstable manifolds. The methodology adopted for the construction of fate maps is described in Section 7, while Sections 8 and 9 provide a dynamical interpretation of the observed behaviours and compare the results obtained for different fate maps. A preliminary assessment of the identified trajectory behaviours and their implications for disposal design is presented in Section 10. Finally, Sections 11 and 12 investigate the evolution of the JC and FTLE fields, respectively, with respect to the patterns visible in the fate maps, while Section 13 summarises the main conclusions and proposed future works.

2 The circular restricted three-body problem and its fundamental properties

The CR3BP model, described by Szebehely (1967), Koon et al. (2011), Gómez et al. (2001), defines the motion of an object with negligible mass in a region of space strongly influenced by the gravitational attraction of two major bodies, which are assumed to be moving in circular orbits around their common Centre of Mass (CoM).

In the classical CR3BP formulation, the state of an object, where $\boldsymbol{r}$ is the position and $\boldsymbol{v}$ is the velocity, is defined in a non-dimensional, rotating coordinate system, having its origin at the primaries' CoM, with the x-axis lying along the direction from the major to the minor primary, and the z-axis orthogonal to the plane of the two bodies' motion. The dimensionless gravitational constant of the EM system, μ_{EM}, is 0.01215, that of the SE system, μ_{SE}, 3.0404×10^{-6}. Lengths are scaled relative to the average EM or SE distances, 384399 km and 149597870.7 km, respectively. Times are scaled such that the average angular velocity of the rotating frames equals 1. Thus, length units are expressed as either LU_{EM} or LU_{SE}, and time units as either TU_{EM} or TU_{SE}. The equations of motion of the classical CR3BP can be expressed as:

$$\begin{cases} \dot{\boldsymbol{r}} = \boldsymbol{v} \\ \dot{\boldsymbol{v}} = 2 \begin{bmatrix} v_y \\ -v_x \\ 0 \end{bmatrix} + \boldsymbol{\nabla}_{\boldsymbol{r}} U(\boldsymbol{r}) \end{cases} \tag{1}$$

with the symbol $\boldsymbol{\nabla}_{\boldsymbol{r}}$ defining the gradient of a function with respect to the variable $\boldsymbol{r}$, and the potential-like function U is defined as:

$$U(\boldsymbol{r}) = \frac{1}{2}(r_x^2 + r_y^2) + \frac{1-\mu}{r_1} + \frac{\mu}{r_2} + \frac{1}{2}\mu(1-\mu) \tag{2}$$

The variables r_1 and r_2 represent the distances between the third body and the two primaries. The major primary is located at $x = -\mu$, while the minor primary is at $x = 1 - \mu$. Accordingly, r_1 and r_2 can be expressed as:

$$r_1 = ((r_x + \mu)^2 + r_y^2 + r_z^2)^{1/2} \tag{3}$$

$$r_2 = ((r_x - 1 + \mu)^2 + r_y^2 + r_z^2)^{1/2} \tag{4}$$

Within the CR3BP, only one integral of motion exists, termed the Jacobi Constant (JC), which is defined as:

$$JC(\boldsymbol{r}, \boldsymbol{v}) = 2\bar{U}(\boldsymbol{r}) - ||\boldsymbol{v}||^2 \tag{5}$$

where $\bar{U}(\boldsymbol{r})$ denotes the potential function $U(\boldsymbol{r})$ with the constant term removed. The JC can be associated with an energy-like constant E, such that $E = -JC/2$, i.e. an increase of the JC corresponds to a decrease of the total energy of the system and vice versa. Five equilibrium points, known as the Libration or Lagrange points L_1 to L_5, can be identified, and the regions of admissible motion for a particle are characterised based on its energy. For a given value of the JC, the motion is constrained to a five-dimensional energy surface embedded in a six-dimensional phase space. The boundaries of the corresponding regions of motion, known as ZVSs, Zero Velocity Curves (ZVCs) when considering planar motion or a planar view, are defined as the loci where the velocity of the particle is zero (see Koon et al. (2011)). In Fig. 1, ZVCs are presented for both the EM and the SE systems, together with the five libration points of the EM system and only the L_1 and L_2 points for the SE one. In the latter case, only a smaller portion of the ZVCs is shown, specifically the region near the system bottlenecks, as this is the area of primary interest for the analysis discussed in the present work. Figure 1 also illustrates how the shape of the curves varies with the value of the JC, whether computed in the EM or SE system.

In the context of the CR3BP, indicators can be used to interpret the dynamical characteristics of the system. Lyapunov exponents have been classically used as a metric related to the chaoticity of a given trajectory by quantifying its sensitivity to small perturbations, i.e. the rate of divergence of initially close solutions (Celletti (2010)). The mathematical definition of Lyapunov exponents can be traced back to Oseledets (1968), and their number equals the dimension of the system, even if typically only

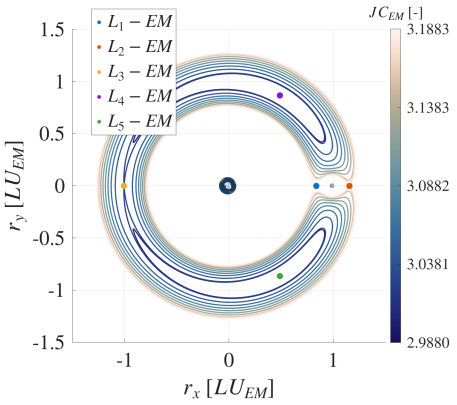

(a) EM ZVCs and EM equilibrium points. The Earth and the Moon are depicted with radii scaled to ten times their actual size for visualisation purposes.

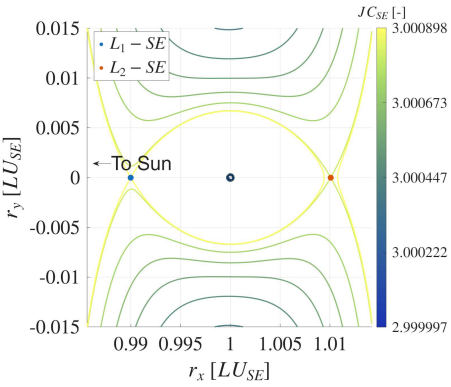

(b) SE ZVCs and SE equilibrium points (L_1 and L_2 only). The Earth is depicted with the radius scaled to ten times its actual size for visualisation purposes.

Fig. 1: ZVCs of the EM and SE systems are shown in their respective rotating reference frames as a function of the JC (computed within either the EM or SE CR3BP). All five equilibrium points are reported for the EM system, while only L_1 and L_2 are shown for the SE system.

the largest or characteristic one is computed, as it provides the maximal excursion associated with nearby orbits. Let us assume that an initial variation $\delta\boldsymbol{x}(t_0)$ on the initial state results in a variation $\delta\boldsymbol{x}(t)$ on the final one, and that the two are connected through the evolution of the state transition matrix of the system, $\boldsymbol{\Phi}(t, t_0)$, such that $\delta\boldsymbol{x}(t) = \boldsymbol{\Phi}(t, t_0)\,\delta\boldsymbol{x}(t_0)$. Lyapunov exponents can be defined as:

$$\Lambda_n = \lim_{t\to\infty} \frac{1}{t} \ln \frac{|\delta\boldsymbol{x}(t)|}{|\delta\boldsymbol{x}(t_0)|} \tag{6}$$

which can also be expressed as:

$$\Lambda_i = \lim_{t\to\infty} \frac{1}{t} \ln |\lambda_i(t)| \qquad i = 1, ..., n \tag{7}$$

where $|\lambda_i(t)|$ are the n normalised eigenvalues of the state transition matrix (Parker and Chua (1989)). In this way, Lyapunov exponents can be used to characterise the chaoticity of the local neighbourhood of the initial point $\boldsymbol{x_0}$. However, this definition

implies knowledge of the system evolution over an infinite time horizon, which, in the cases described in this work, may not be readily available. Finite Time Lyapunov Exponents (FTLEs) provide a relative measure of the growth or contraction of the elements of the phase space over a defined characteristic time, as described for instance in Short (2016), and they can be interpreted as a finite time truncation of classical Lyapunov exponents. The maximum FTLE (identified from now on simply as the FTLE), $L(t^*)$, can be computed as:

$$L(t^*) = \frac{1}{t^*} \ln(\lambda_{max}) \tag{8}$$

where λ_{max} is the maximum eigenvalue of the square root of the Cauchy-Green tensor, $\boldsymbol{C} = \boldsymbol{\Phi}^T(t^*, t_0)\, \boldsymbol{\Phi}(t^*, t_0)$, and t^* is the characteristic final time to which a certain value of FTLE is related. The FTLE provides a measure of the effect a perturbation would have on the system over finite times: the higher the FTLE, the higher the effect of such a perturbation on the system is when applied at a selected point and with reference to a certain characteristic time. Note that high FTLE values are also associated with conditions in which the two major bodies in the system have a similar effect on the trajectory behaviour and with points where a manoeuvre would have a stronger effect on its evolution (see Anderson et al. (2003)). When considering a field of FTLE values on a map or section, height ridges corresponding to relatively large FTLE values may also represent Lagrangian coherent structures. These structures act as separatrices between regions exhibiting different qualitative behaviour, as discussed for instance by Short (2016) and by Canales and Howell (2024).

3 Coupled circular restricted three-body problem

The dynamical model used in the analysis is the EM and SE coupled CR3BP. In the case of the coupled CR3BP, described for example by Castelli (2011), the two main bodies involved are either the Earth and the Moon, or the Sun and the Earth,

depending on which of the two, the Moon or the Sun, has a stronger influence on the trajectory. In the coupled CR3BP, the two CR3BP models are approximated as coplanar, and they are linked via a coordinate change and the evolution of their relative phase over time, as detailed by Castelli (2011). Let us define the phase of the EM system relative to the SE system at a generic instant t as $\alpha(t)$, shown in the left panel of Fig. 2.

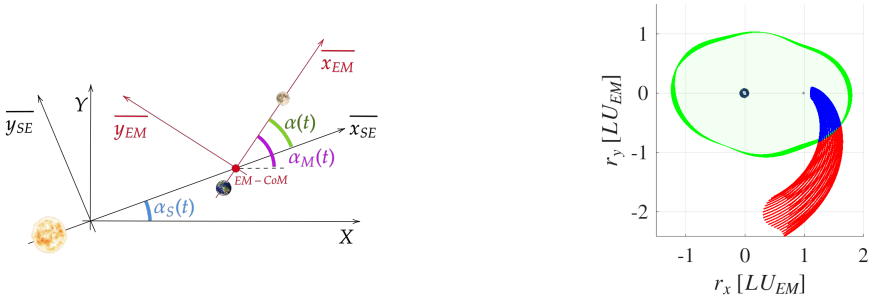

Fig. 2: Left: Schematic representation of the coupled CR3BP. Right: Evolution of unstable manifold trajectories departing from a Halo orbit around EM-L_2 in the coupled CR3BP, propagated for 1 month, with $\alpha_0 = 0°$. Blue and red segments indicate trajectory states governed by the EM and SE CR3BP dynamics, respectively. The green region corresponds to the domain where the EM CR3BP prevails. The Earth and the Moon are depicted with radii scaled to five times their actual size for visualisation purposes.

The angle $\alpha(t)$ is used to determine the geometric relationship between the two systems at any time, with its evolution given by:

$$\alpha(t_{EM}) = \alpha_0 + \frac{\omega_{EM} - \omega_{SE}}{\omega_{EM}} t_{EM} \tag{9}$$

where ω_{EM} and ω_{SE} are the non-dimensional angular velocities of the two rotating frames, fixed at 2.6653×10^{-6} and 1.9909×10^{-7}, t_{EM} is the propagation time in the EM system, and α_0 is the relative phase between the two models at the instant in which the spacecraft is inserted into the trajectory. In the coupled CR3BP, a trajectory leaving an LPO of the EM system is propagated considering only the EM CR3BP until the influence exerted by the Moon on the spacecraft is less than that exerted by

the Sun. At this point, the dynamical model switches to the SE CR3BP. The relative influence of each CR3BP on the trajectory evolution is evaluated by determining, at each instant, which of the two models yields the lowest error when used in place of the bicircular restricted four-body problem (Castelli (2011)). The right panel of Fig. 2 shows a selection of unstable manifold trajectories computed within the coupled CR3BP framework, propagated for 1 month. Trajectory segments governed by the EM CR3BP are shown in blue, whereas those governed by the SE CR3BP are shown in red. The green region identifies the domain in which the EM CR3BP prevails. The dynamics are modelled as switching between the EM and SE CR3BP as many times as necessary, considering at each time step only either the EM or the SE CR3BP. This formulation, which was applied in the past, for instance, to lunar impact disposal for spacecraft departing from LPOs in the SE system by Van der Weg and Vasile (2014), has the advantage of completely decoupling the effect of the Sun on the trajectory from that of the Moon while preserving all the fundamental quantities of the CR3BP, thereby facilitating an effective dynamical interpretation of the results. It also allows for simple potential extensions of the model, such as the inclusion of the Moon's inclination with respect to the ecliptic within the dynamical framework. Note that the coupled CR3BP is an autonomous dynamical model, since its equations of motion are time-independent. However, the coordinate transformation between the EM and SE frames depends on $\alpha(t)$ and is therefore non-autonomous.

Finally, Fig. 3 presents the ZVCs of the EM and SE systems within the coupled CR3BP, for the case of $\alpha = 0°$.

The ZVCs and forbidden regions of the SE and EM systems are shown in green and red, respectively, and are evaluated at the JC corresponding to the respective L_2 points. The region of space extending from 150 km above the Earth's surface to EM-L_2 is, in this work, generically identified as cislunar (purple in Fig. 3). The

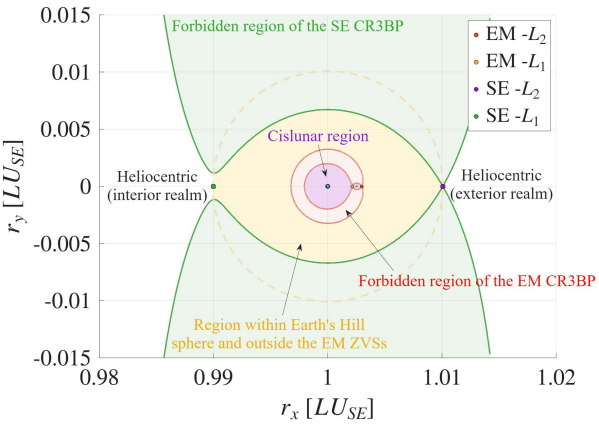

Fig. 3: SE and EM ZVCs in the SE system, evaluated at the JC of SE-L_2 and EM-L_2, respectively. The L_1 and L_2 points of both systems are also represented. The Earth and the Moon are depicted with radii scaled to ten times their actual size for visualisation purposes. The different regions of the Sun-Earth-Moon system are classified according to the definitions that will be adopted throughout this work.

region within Earth's Hill sphere and outside the EM ZVSs is identified using its extended definition (yellow in Fig. 3). Finally, the regions beyond the SE-L_1 and SE-L_2 bottlenecks are classified as interior and exterior heliocentric regions, respectively. It should be noted that, at present, the terminology used to identify the different regions of the Sun-Earth-Moon system is not uniformly adopted across the scientific community. Consequently, the naming convention adopted in this work is not intended as a reference or recommendation for future studies. The classification introduced here is used solely for the purpose of improving the readability and interpretation of the fate or outcome maps presented in the following sections, as a comprehensive discussion on the most appropriate terminology for the various regions of the Sun-Earth-Moon system lies beyond the scope of this work and is being addressed in greater detail by other studies.

4 Transformation from the rotating to the J2000 reference frame

For some of the analysis presented in this work, a transformation from the EM rotating reference frame to the Earth-centred J2000 inertial reference frame is performed. The x-axis of the J2000 inertial reference frame is defined by the intersection of the Earth's equatorial plane and the ecliptic plane, i.e. the vernal equinox at epoch J2000. The z-axis is normal to the mean Earth's equator at epoch J2000, while the y-axis completes the right-handed triad. The central body is the Earth. A strategy similar to that discussed by Gómez et al. (2001), and later by Nicolás Ávila (2022), is adapted to the specific case at hand. Note that this transformation is ephemeris-based, i.e. time-dependent, and accounts for the roto-pulsating effects arising from both the rotation of the original reference frame relative to the inertial frame and the time-varying distance between the primaries. Let $\boldsymbol{r}$ be the position of a point in a rotating reference frame and $\hat{\boldsymbol{r}}$ that same position in the Earth-centred J2000 inertial frame. Quantities related to the major body of the reference CR3BP are identified by the number 1, quantities related to the minor body by the number 2. The transformation of the position can be described as:

$$\hat{\boldsymbol{r}} = k\boldsymbol{C}\boldsymbol{r} + \boldsymbol{b} \tag{10}$$

where $k = ||\boldsymbol{R_2} - \boldsymbol{R_1}||$ is a scaling factor, and $\boldsymbol{R_2}$ and $\boldsymbol{R_1}$ are the positions of the minor and major bodies of the reference CR3BP, respectively, expressed in the J2000 reference frame centred at the rotating-frame origin and obtained from the DE440 ephemeris kernel through the NASA SPICE toolkit (see NASA SPICE (2025)). The vector $\boldsymbol{b}$ shifts the origin of the system from the rotating frame centre to either the Earth, while the matrix $\boldsymbol{C}$ is an orthonormal matrix representing the rotation from

the rotating reference frame to the inertial reference frame, $\boldsymbol{C} = [\boldsymbol{c_1}\ \boldsymbol{c_2}\ \boldsymbol{c_3}]$. The components of the matrix $\boldsymbol{C}$ can be computed as:

$$\boldsymbol{c_1} = \frac{\boldsymbol{R}}{k} \qquad \boldsymbol{c_3} = \frac{\boldsymbol{R} \times \boldsymbol{V}}{||\boldsymbol{R} \times \boldsymbol{V}||} \qquad \boldsymbol{c_2} = \boldsymbol{c_3} \times \boldsymbol{c_1} \tag{11}$$

where $\boldsymbol{R} = \boldsymbol{R_2} - \boldsymbol{R_1}$ and $\boldsymbol{V} = \boldsymbol{V_2} - \boldsymbol{V_1}$. The relationship between the velocity in one of the rotating frames, $\boldsymbol{v}$, and that in the Earth-centred J2000 frame, $\hat{\boldsymbol{v}}$, can be obtained by differentiating Eq. 10 with respect to time (see Gómez et al. (2001) and Nicolás Ávila (2022) for further details).

5 Periodic orbits selected as test cases for the analysis

The reference LPOs selected as test cases for the analysis presented in this work are four Halo orbits and two NRHOs: three centred at EM-L_1 and three at EM-L_2. Numerous families of periodic orbits can be defined in a three-body system, as detailed, for instance, by Doedel et al. (2007). Periodic orbits are solutions of the classical CR3BP and originate from one of the system's libration points or, secondarily, from other families of periodic orbits. Given an initial guess close to the bifurcation point from which the family of periodic orbits originates, a single orbit is first computed using a differential correction algorithm that enforces periodicity, orthogonality, and symmetry with respect to a given reference plane, Koon et al. (2011). Subsequently, the initial guesses required to generate the remaining members of the family are obtained through continuation algorithms, and differential corrections are applied to find the number of members in the family required by the analysis.

The Halo families constitute only one class of LPOs which can be defined in the EM CR3BP; however, they are among the most relevant for future applications. NRHOs represent a subset of the Halo families and are characterised by a close approach to the Moon at perilune, greater stability than other orbits belonging to the Halo families, and

a highly elongated geometry. These characteristics make them particularly attractive as reference orbits for future cislunar mission architectures aiming to study or reach the lunar surface. The six LPOs chosen as test cases for the analysis are reported as a function of the phase angle in Fig. 4, in two different views: they are two Halos and one NRHO in EM-L_2 and their counterparts in EM-L_1. The red marker in Fig. 4 represents EM-L_2, the blue marker EM-L_1.

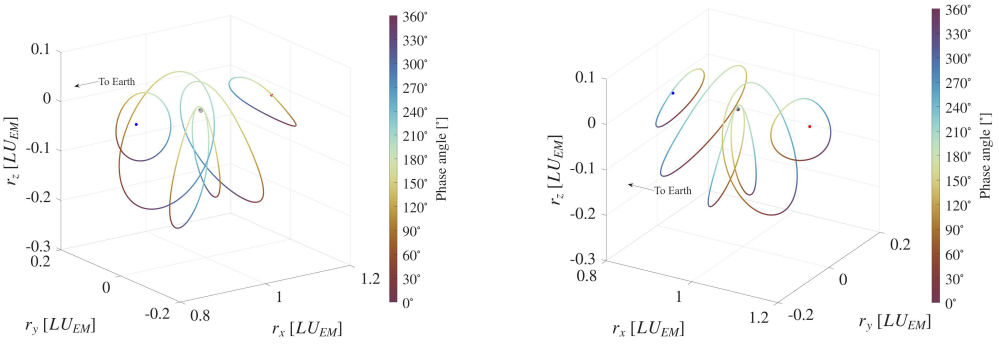

Fig. 4: LPOs selected as test cases for the analysis, represented as a function of the phase angle in two different views.

The phase angle, θ_0, is a parametrisation of the time the spacecraft takes to complete one revolution of the periodic orbit, such that:

$$\theta_0 = 2\pi \frac{t}{T} \tag{12}$$

where t is a generic Time of Flight (ToF) and T is the LPO's period. The phase angle is equal to 0° (or equivalently 360°) at the intersection between the periodic orbit and the $x-z$ plane corresponding to negative r_z values (generally the apolune), and equal to 180° at the intersection corresponding to positive r_z values (generally the perilune). The selected NRHO associated with EM-L_2 is chosen because of its similarity to the 9:2 NRHO adopted as the reference orbit for the Lunar Gateway. The other five selected orbits are not associated with any specific mission but are chosen to provide reference results and to illustrate how behaviours related to EoL disposal

in cislunar space can be mapped across the Halo families. The analysis presented here may subsequently be extended to other specific orbits, to the entire Halo family, and to other families of periodic orbits. The characteristics of the six test cases are reported in Tab. 1, together with the Id identifying each of them, and their initial conditions in Tab. 2.

Table 1: Characteristics of the LPOs selected as candidates for the analysis: JC, stability index, perilune radius and period.

Orbit type	Id	JC [-]	SI [-]	r_p [km]	T [days]
Halo in EM-L_2	**A2**	3.1382	472.5598	48796.88	14.75
	B2	3.0168	3.9950	20981.70	11.15
NRHO in EM-L_2	**C2**	3.0488	1.3021	2932.67	6.45
Halo in EM-L_1	**A1**	3.1385	614.2841	48013.71	12.06
	B1	3.0162	19.3740	32131.85	11.47
NRHO in EM-L_1	**C1**	2.9960	2.6996	2939.23	7.95

Table 2: Initial conditions related to the LPOs selected as candidates for the analysis.

Orbit type	Id	x_0 $[LU_{EM}, LU_{EM}/TU_{EM}]$
Halo in EM-L_2	**A2**	$x_0 = [1.177317 \quad 0 \quad -0.057409 \quad 0 \quad -0.172415 \quad 0]$
	B2	$x_0 = [1.094807 \quad 0 \quad -0.200644 \quad 0 \quad -0.211917 \quad 0]$
NRHO in EM-L_2	**C2**	$x_0 = [1.019805 \quad 0 \quad -0.180521 \quad 0 \quad -0.098377 \quad 0]$
Halo in EM-L_1	**A1**	$x_0 = [0.824772 \quad 0 \quad -0.067764 \quad 0 \quad 0.179743 \quad 0]$
	B1	$x_0 = [0.844910 \quad 0 \quad -0.168216 \quad 0 \quad 0.264140 \quad 0]$
NRHO in EM-L_1	**C1**	$x_0 = [0.929261 \quad 0 \quad -0.226490 \quad 0 \quad 0.108746 \quad 0]$

Orbits A2 (associated with EM-L_2) and A1 (associated with EM-L_1) are located close to their respective Libration points and are characterised by high Stability Index (SI) values and large perilune radii. The SI is a measure of the linear stability of a periodic orbit and is computed as (e.g. Gómez et al. (2001)):

$$SI = \frac{1}{2}\left|\left(\lambda_{max} + \frac{1}{\lambda_{max}}\right)\right| \tag{13}$$

where λ_{max} is the largest eigenvalue of the monodromy matrix, i.e. the state transition matrix evaluated over one orbital period. A periodic orbit is classified as linearly stable when $SI \leq 1$, e.g. Howell (1984). Both A2 and A1 are, in fact, highly unstable. These two orbits have been selected as representative cases of trajectories located close to their respective libration points, whose dynamics during the initial phase of the EoL disposal are less strongly influenced by the Moon than those associated with the other LPOs. They are characterised by similar initial energy levels, distances from the Moon, geometrical shapes, and stability properties, thereby facilitating a preliminary comparison between the dynamical behaviours related to orbits centred around EM-L_1 and EM-L_2. Orbits B2 and B1 have been selected with the same logic, having similar energy levels, and are much closer to the Moon, i.e., have lower perilune radii, with respect to A2 and A1. They are also closer to a stable condition and are characterised by higher energy levels. Orbits C1 and C2, on the other hand, are proper NRHOs, i.e. they are characterised by very low perilune radii, high stability, and relatively high energy levels compared with the majority of the other orbits in the family. For a complete definition of NRHOs, see, for example, Zimovan-Spreen et al. (2020). As stated previously, orbit C2 is similar to the 9:2 NRHO adopted as the reference orbit for the Lunar Gateway, while orbit C1 was selected to have the same perilune radius as C2. Considering all six orbits together makes it possible to analyse the dynamics of three very different regions of the Halo family, thus providing the most comprehensive view possible with a limited number of test cases.

6 Unstable manifolds associated with periodic orbits

Disposal trajectories are computed by initially inserting the spacecraft onto the unstable manifolds of the reference periodic orbits. The unstable manifold direction is

regarded as the most effective direction for disposal, as it corresponds to the motion that asymptotically diverges from the reference orbit. This assumption is valid for linearly unstable periodic orbits, i.e. those characterised by $SI > 1$, such as the cases analysed in this work. The situation would be different for linearly stable LPOs, which are not considered in the present analysis.

The unstable manifold direction at $\theta_0 = 0°$ and time $t_0 = 0$, denoted by $\boldsymbol{W^u}(0)$, is defined as the eigenvector associated with the largest real eigenvalue of the monodromy matrix, λ_{max}. The unstable manifold direction associated with any other phase angle, $\boldsymbol{W^u}(\theta_0)$, is mapped through the evolution of the state transition matrix of the periodic orbit, $\boldsymbol{W^u}(\theta_0) = \boldsymbol{\Phi}(t, t_0)\boldsymbol{W^u}(0)$. By normalising $\boldsymbol{W^u}(\theta_0)$, the local linear approximation of the unstable manifold direction, $\hat{\boldsymbol{W}}^{\boldsymbol{u}}(\theta_0)$, is obtained. The initial condition of a trajectory on the unstable manifold for a generic value of θ_0, denoted by $\boldsymbol{x_0^u}(\theta_0)$, can be computed as:

$$\boldsymbol{x_0^u}(\theta_0) = \boldsymbol{x_0}(\theta_0) \pm \varepsilon\, \hat{\boldsymbol{W}}^{\boldsymbol{u}}(\theta_0) \tag{14}$$

where $\boldsymbol{x_0}(\theta_0)$ is the state of the periodic orbit corresponding to a given value of θ_0, and ε is a perturbation large enough to allow the spacecraft to depart from the reference periodic orbit, yet small enough to preserve the validity of the linear approximation. For the EM system, this parameter typically ranges between 10^{-6} and 10^{-4}. In this work, a value of $\varepsilon = 10^{-4}$ is adopted. The parameter ε can be physically interpreted as a perturbation applied to the nominal state of the periodic orbit, with a variation with respect to the nominal position of 38.43 km and one with respect to the nominal velocity of about 10 cm/s. It should be emphasised that the manifold parametrisation is not independent of ε: changes in its value lead to a rotation of the manifold along θ_0. Furthermore, ε affects the characteristic escape timescale, with larger perturbations generally yielding a more rapid divergence from the reference orbit. As shown in Fig. 5,

and as can be inferred from Eq. 14, each periodic orbit is associated with two unstable manifold branches.

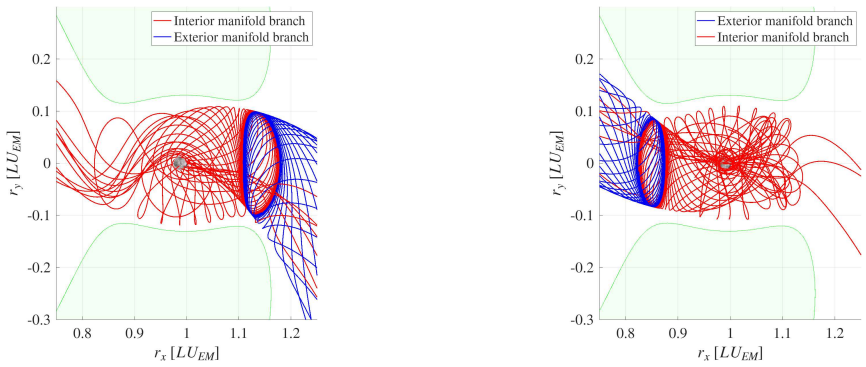

Fig. 5: Exterior (blue) and interior (red) unstable manifold branches departing from the reference Halo orbits A2 (left) and A1 (right), propagated for 1 month. The Moon's radius has been scaled to three times its size for visualisation purposes. In green, the ZVCs of the EM system are evaluated at the JC of the reference Halo orbit.

Typically, especially in the case of highly linearly unstable orbits, one branch, referred to as the exterior manifold and shown in blue in Fig. 5, is directed towards the bottleneck region around the corresponding libration point of the EM system. The other branch, referred to as the interior manifold and shown in red in Fig. 5, is directed towards the Moon. In other words, the structure formed by manifold trajectories can be viewed as a tube from a topological perspective. This property holds as long as the largest real eigenvalue of the monodromy matrix, λ_{max}, is positive, since

$$\boldsymbol{W^u}(2\pi) = \boldsymbol{\Phi}(T, t_0)\boldsymbol{W^u}(0) = \lambda_{max}\boldsymbol{W^u}(0) \tag{15}$$

where $\boldsymbol{\Phi}(T, t_0)$ denotes the monodromy matrix. This implies that both the direction and the orientation of $\boldsymbol{W^u}(2\pi)$, i.e. the unstable manifold direction after one period of the periodic orbit, are identical to those of $\boldsymbol{W^u}(0)$ if λ_{max} is positive. Instead, in the case of a negative λ_{max}, the unstable manifold directions at $\theta_0 = 0$ and $\theta_0 = 2\pi$ have the same direction but opposite orientation. This is the case for NRHOs which

are unstable in the linear sense, having a $SI > 1$, including the ones considered in this work. It is known that the directions of the manifolds of NRHOs are not well defined Boudad et al. (2022) and, indeed, knowing that $\boldsymbol{W^u}(2\pi) = \lambda_{max}\boldsymbol{W^u}(0)$, having a negative value of λ_{max} results in a reversal of the orientation of the unstable eigenvector after one orbital period. For further information on the evolution of λ_{max} within the NRHOs family, refer to Boudad et al. (2022) and to Bolis et al. (2026a). In the case of C2, for example, λ_{max} is about -2.0252. Note that, apart from this, the eigenvalues of the monodromy matrix exhibit the classical structure associated with linearly unstable LPOs: one eigenvalue is real and has modulus greater than one, a second eigenvalue is its reciprocal, the third and fourth eigenvalues form a complex conjugate pair, and the remaining two eigenvalues are equal to unity. It is also known that the state transition matrix expressed in canonical coordinates is symplectic. Following the procedure described in detail by Williams (2024), the state transition matrix in canonical coordinates, $\boldsymbol{\Psi}(t, t_0)$, can be derived from the state transition matrix in rotating coordinates, $\boldsymbol{\Phi}(t, t_0)$, as

$$\boldsymbol{\Psi(t, t_0)} = \boldsymbol{T}\,\boldsymbol{\Phi}(T, t_0)\,\boldsymbol{T}^{-1} \tag{16}$$

where

$$\boldsymbol{T} = \begin{bmatrix} \boldsymbol{I_{3x3}} & \boldsymbol{0_{3x3}} \\ \boldsymbol{\Omega} & \boldsymbol{I_{3x3}} \end{bmatrix} \qquad \textit{and} \qquad \boldsymbol{\Omega} = \begin{bmatrix} 0 & -1 & 0 \\ 1 & 0 & 0 \\ 0 & 0 & 0 \end{bmatrix} \tag{17}$$

Consequently, to assess the accuracy of the computed monodromy matrix, it was verified that, for the cases analysed,

$$\boldsymbol{\Psi}(\boldsymbol{T}, \boldsymbol{t_0})\, \boldsymbol{J}\, \boldsymbol{\Psi}(\boldsymbol{T}, \boldsymbol{t_0}) - \boldsymbol{J} = 0 \qquad with \qquad \boldsymbol{J} = \begin{bmatrix} \boldsymbol{0_{3x3}} & \boldsymbol{I_{3x3}} \\ -\boldsymbol{I_{3x3}} & \boldsymbol{0_{3x3}} \end{bmatrix} \tag{18}$$

which is satisfied, with a residual error of the order of 10^{-12}. Summarising, since λ_{max} is negative for the NRHOs considered in this work, their unstable manifold is non-orientable. From a topological perspective, it can therefore be regarded as a Möbius strip, a behaviour described as a general property of manifolds of three-dimensional vector fields by Osinga (2000) and Osinga (2003). The unstable manifold related to C2 is represented in Fig. 6. It should be noted that what has been discussed regarding C2 also applies to C1, whose maximum eigenvalue is approximately -5.2071.

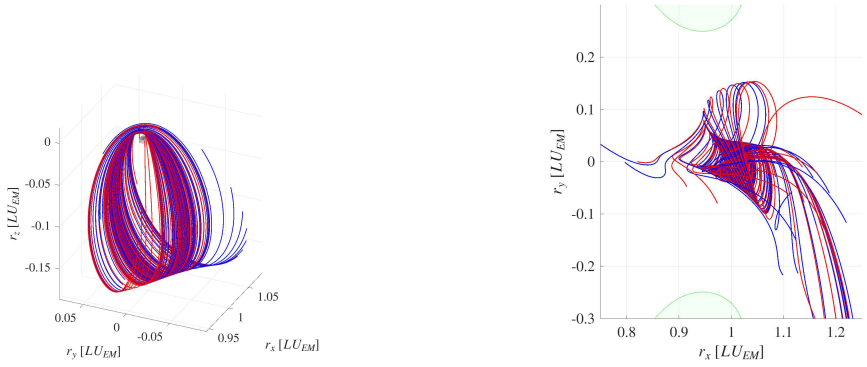

Fig. 6: Unstable manifold branches (blue and red) departing from the reference NRHO C2, propagated for 60 days (left) and 75 days (right). In green in the graph on the right, the ZVCs of the EM system are evaluated at the JC related to C2.

7 Methodology for the construction of fate maps

The analyses presented in this work investigate how the outcomes of unstable manifold propagation in the coupled CR3BP evolve as the departure conditions from LPOs are progressively varied. These conditions are defined by θ_0, the phase angle on the

periodic orbit associated with a given unstable manifold trajectory initial condition, as shown in Fig. 4, and α_0, the phase of the EM system relative to the SE system at the time of departure from the periodic orbit (see Eq. 9). A discretisation step of 2° is adopted for both parameters. Trajectory propagation is performed using MATLAB's built-in integrator `ode113`, with a maximum propagation time of 12 months. Other numerical integrators commonly employed for CR3BP applications are also tested, and the resulting trajectories show only minor differences with respect to those obtained using `ode113`. The relative and absolute tolerances are set to 2.22045×10^{-14} and 10^{-16}, respectively, corresponding to the smallest values allowed by the algorithm. The final state of each unstable manifold trajectory can be classified as:

- located in the heliocentric exterior region, i.e. the satellite escapes through SE-L_2 (blue in the fate maps);
- located in the heliocentric interior region, i.e. the satellite escapes through SE-L_1 (green in the fate maps);
- it reaches the Moon surface, i.e. the satellite impacts the Moon (purple in the fate maps);
- it reaches an altitude less than 150 km above the Earth's surface, i.e. the satellite re-enters the Earth's atmosphere (red in the fate maps);
- located in the region within Earth's Hill sphere and outside the EM ZVSs, i.e. the satellite goes through the EM-L_2 bottleneck without subsequently escaping through either the SE-L_1 or SE-L_2 bottleneck, without impacting any body, and with its final state located in the region within Earth's Hill sphere and outside the EM ZVSs (yellow in the fate maps); or
- located in the cislunar region, i.e. the spacecraft either remains within the EM system without escaping through the EM-L_2 bottleneck and without impacting any body, or the spacecraft escapes from the EM-L_2 bottleneck, orbits the region within Earth's Hill sphere and outside the EM ZVSs, for then re-entering the EM ZVSs

at a later stage, with its final state located in the cislunar region (white in the fate maps).

In the case of a Moon impact or Earth re-entry, the propagation terminates at impact. For all other outcomes, the maps indicate the region of space where the trajectory is located at the end of the propagation. It is important to highlight that the maps represent only the location of the final state of a trajectory. In other words, for instance, a final state classified as located in the region within Earth's Hill sphere and outside the EM ZVSs may be generated either by a trajectory that escapes the cislunar region and subsequently re-enters the EM ZVSs, possibly also approaching the Earth or the Moon, or by a trajectory that never re-enters the EM ZVSs during the entire propagation interval considered.

8 Fate map of the exterior unstable manifold branch of the Halo orbit A2

The results obtained with reference to the exterior manifold branch of orbit A2 are reported in Fig.7.

Let us first start by observing the evolution of trajectories' fates along θ_0. No clear symmetry can be identified. This can be attributed to the geometry of the unstable manifold departing from the LPOs when considering the EM CR3BP only (see, for instance, Bolis et al. (2026b) for further details on the evolution of the exterior unstable manifold branch of EM-L_2 Halo orbits in the EM CR3BP). Anyway, two distinct dynamical regimes clearly emerge as θ_0 evolves. Referencing Fig. 7, the first extends approximately for $\theta_0 \in [30°, 270°]$ and is characterised by a relatively homogeneous behaviour, with most trajectories reaching the heliocentric region (either interior or exterior depending on the value of α_0). Within this region, a distinct structure consistently corresponding to Earth re-entries for specific values of α_0 can also be observed.

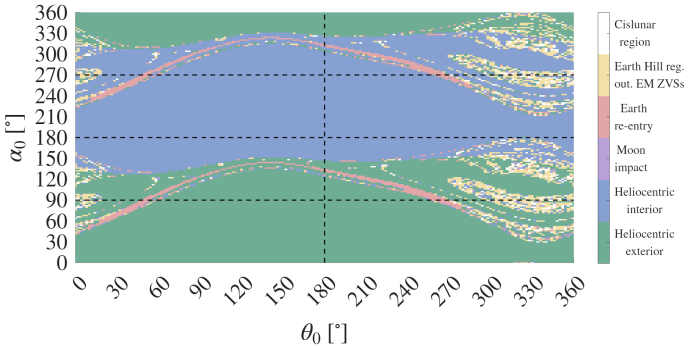

Fig. 7: Fate map obtained from the propagation of the unstable manifold of the reference Halo orbit A2, exterior branch, as a function of θ_0 and α_0. In the maps, blue indicates trajectories reaching the heliocentric exterior region, green indicates trajectories reaching the heliocentric interior region, purple denotes Moon impacts, red denotes Earth re-entries, yellow indicates trajectories whose final state lies in the region within Earth's Hill sphere and outside the EM ZVSs, and white indicates trajectories whose final state lies in the cislunar region.

The second regime, found approximately for $\theta_0 \in [0°, 30°]$ and $\theta_0 \in [270°, 360°]$, exhibits a more irregular and less homogeneous behaviour, with a significant number of trajectories remaining within the EM system and ending in the cislunar region or in the region within Earth's Hill sphere and outside the EM ZVSs. The association of a specific range of values of θ_0 with a particular dynamical regime depends on the initial perturbation ε used to place an object on the unstable manifold of the reference orbit since, as discussed in Section 6, the manifold initial conditions shift with respect to θ_0 as the value of ε is varied. In other words, the range of θ_0 values associated with the homogeneous dynamical behaviour in Fig. 7 moves along the phase angle domain depending on the selected value of ε. This dependence implies that, if the objective is to map the entire solution space, fate maps should depend on three variables rather than two, the third being the initial perturbation ε, or an eventual initial ΔV used to insert the spacecraft on an unstable manifold. Àngel Jorba and Nicolás (2020) present a similar analysis, obtaining fate maps relating θ_0 to ε, associated with a different application, while Guardabasso (2023) proposes the use of fate maps extended

beyond the linear unstable manifold approximation, considering initial ΔV in the tangential direction in the order of $1 - 100$ m/s to depart from the initial LPO. That said, this aspect will not be addressed in the present work. However, it is important to highlight it as a possible limitation and potential future area of study.

The reason why some regions of the fate maps exhibit a homogeneous tendency toward escape (hereafter referred to as Region 1), whereas others display a more varied dynamical behaviour (Region 2), can be traced back to the degree of hyperbolicity with respect to the Earth exhibited by the trajectories during the early stages of their evolution. As an example, consider Fig. 8, which illustrates the evolution of the eccentricity with respect to Earth for trajectories belonging to the exterior branch of the unstable manifold associated with orbit A2, as a function of θ_0 and a ToF. The eccentricity is computed by considering the manifold evolution within the EM CR3BP only, thus neglecting the influence of the Sun. For each state along the trajectory, the Cartesian state vector is first rotated in the Earth-centred J2000 reference frame and then converted into the corresponding Keplerian elements, from which the eccentricity is retrieved.

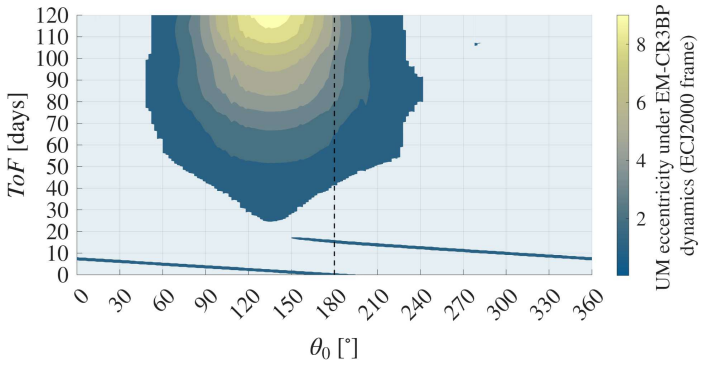

Fig. 8: Evolution of the eccentricity with respect to Earth of trajectories belonging to the exterior branch of the unstable manifold associated with orbit A2, computed considering the EM CR3BP only.

The eccentricity is shown in light blue for values lower than 1, while values greater than 1 are represented according to the adopted colourmap. What clearly emerges is that Region 1 in Fig. 7 corresponds to trajectories that attain high eccentricity values early in their evolution, even when only the EM CR3BP dynamics are considered. In other words, the trajectories associated with the fates observed in Region 1 become rapidly hyperbolic with respect to the Earth. This behaviour is already evident in the EM CR3BP, indicating that the tendency of these trajectories to reach the heliocentric region is primarily driven by the underlying EM dynamics. Note that the eccentricity peaks observed for all values of θ_0 at ToFs shorter than about 20 days are indicative of close approaches to the Moon. In this phase, the dynamics still closely follow those of the reference orbit, as the trajectories have not yet significantly diverged from it.

When observing the fate maps' evolution along α_0, the first feature emerging is their symmetry with respect to $\alpha_0 = 180°$. Referencing Fig. 7 again, a given set of initial conditions with α_0 between 0° and 180° generally leads to escape towards the heliocentric exterior region, whereas the corresponding conditions with α_0 between 180° and 360° tend to evolve towards the heliocentric interior region. Apart from the escape behaviour, which is reversed, the remaining features of the map are largely preserved between the two halves of the α_0 domain. This behaviour is consistently observed across all the cases analysed and can be regarded as a consequence of the underlying structure of the dynamical model itself (see, for instance, the discussion about the symmetry in the evaluation of the Jacobi integral given by García and Gómez (2007)).

As already highlighted in previous studies, such as that by Boudad et al. (2022), the quadrant in which a trajectory is located with respect to the Earth, in the SE rotating frame, when the Sun's gravitational influence becomes non-negligible, plays a fundamental role in determining its fate. Following the quadrant definition provided,

for instance, in Davis (2011) and in Boudad et al. (2022), and reported for clarity in Fig. 9, it is well known that the acceleration induced by the Sun's gravitational perturbation, often referred to as tidal acceleration, in the vicinity of the smaller primary of a three-body system tends to elongate the orbit and decrease the periapsis radius when an apogee of the trajectory is located in the I or III quadrant. In contrast, the same tidal acceleration tends to circularise the orbit when the apogee lies in the II or IV quadrant.

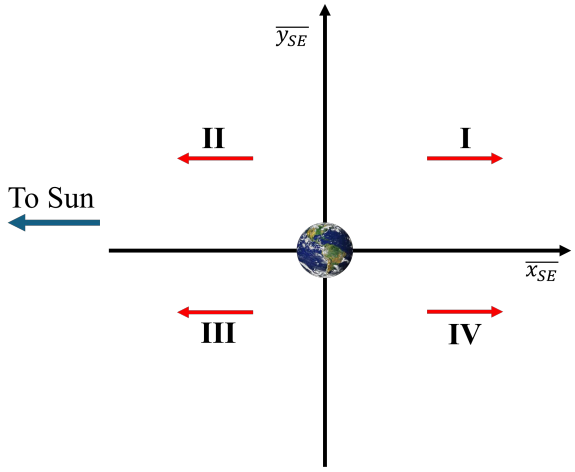

Fig. 9: Schematic representation of the quadrant definition in the rotating SE reference frame. The red arrows indicate the direction of the solar tidal acceleration in the vicinity of the Earth within each quadrant.

Focusing once again on the exterior branch of the unstable manifold associated with orbit A2, Fig. 10 presents, on the left, the quadrant occupied by each trajectory when it first transitions from the EM to the SE CR3BP, shown as a function of θ_0 and α_0. On the right, the figure reports the quadrant in which the first apogee of the trajectory is located, whenever such an apogee exists, again as a function of θ_0 and α_0. It should be noted that apogees are identified as points at which the first time derivative of the Earth-relative distance of an object is equal to zero, while the corresponding second time derivative is negative. In other words, they correspond to local maxima of the

distance from the Earth along the trajectory in the rotating frame. In both figures, the black lines delineate the boundaries between the regions associated with the different trajectory outcomes, as defined in Fig. 7.

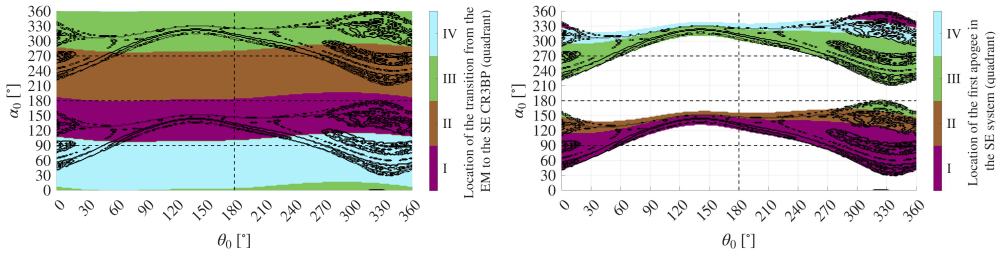

(a) Map showing the quadrant in which the first transition of each trajectory from the EM CR3BP to the SE CR3BP occurs, as a function of θ_0 and α_0.

(b) Map showing the quadrant in which the first apogee of each trajectory is reached, when present, as a function of θ_0 and α_0.

Fig. 10: Illustration of the relationship between the position of a trajectory in the SE system (in terms of quadrants) and its outcome. The black lines correspond to the boundaries related to different outcomes which can be identified in the associated fate maps of the exterior branch of the unstable manifold of orbit A2.

By examining the map on the left side of Fig. 10, it is clear that trajectories transitioning from the EM to the SE CR3BP while located in the II or IV quadrant are generally associated with the central portions of the regions characterised by a consistent tendency toward reaching the heliocentric region, particularly within the range of θ_0 previously identified as Region 1. Trajectories that transition between the two dynamical regimes while located in the I or III quadrant tend to exhibit a wider variety of outcomes, even within Region 1. This becomes especially evident when considering the quadrant in which their first apogee is reached, which is found to be the I or the III, particularly when they relate to Earth re-entries. This behaviour is primarily governed by α_0 in combination with the ToF, as these parameters determine the quadrant occupied by the trajectory at the instant when the Sun's gravitational influence becomes dominant over that of the Earth.

As a final remark, although the results presented here refer to orbit A2, the same

underlying behaviours have been observed across all the cases analysed, subject to the specific variations that will be discussed in the following section. These additional results are not presented here for the sake of brevity.

9 Comparison of the fate maps associated with the selected orbits

The results obtained for both the interior and exterior manifold branches of the selected LPOs related to EM-L_2 are reported in Fig. 11.

Let's start by observing in greater detail the fate maps related to, again, orbit A2, Fig. 11a and Fig. 11b. A2 has the smallest amplitude among the LPOs analysed and is the closest to EM-L_2. The behaviour observed for both its unstable manifold branches is the most regular among the ones studied. The exterior branch clearly leads to a large number of heliocentric trajectories, whereas the interior branch results in a large number of Moon impacts. This is due both to the high linear instability associated with A2, which causes its unstable manifolds to depart rapidly from the reference periodic orbit, and to its small out-of-plane amplitude. The limited extent of A2 along the z direction implies that its manifolds are also nearly planar, naturally increasing the likelihood of a Moon impact compared with orbits characterised by a larger vertical amplitude. In Fig. 11b, cases in which a cislunar condition is reached for a given value of θ_0 and for all values of α_0 correspond to trajectories that never escape the EM ZVSs.

As regards orbit B2, which is closer to the Moon and has a greater amplitude along the z-axis, the behaviour of the unstable manifold becomes less regular, with impacts on the Moon being almost non-existent even for the inner branch of the unstable manifold, as shown in Fig. 11c and Fig. 11d. This orbit is also located very close to the stable region of the Halo family, from which a period-doubling bifurcation arises.

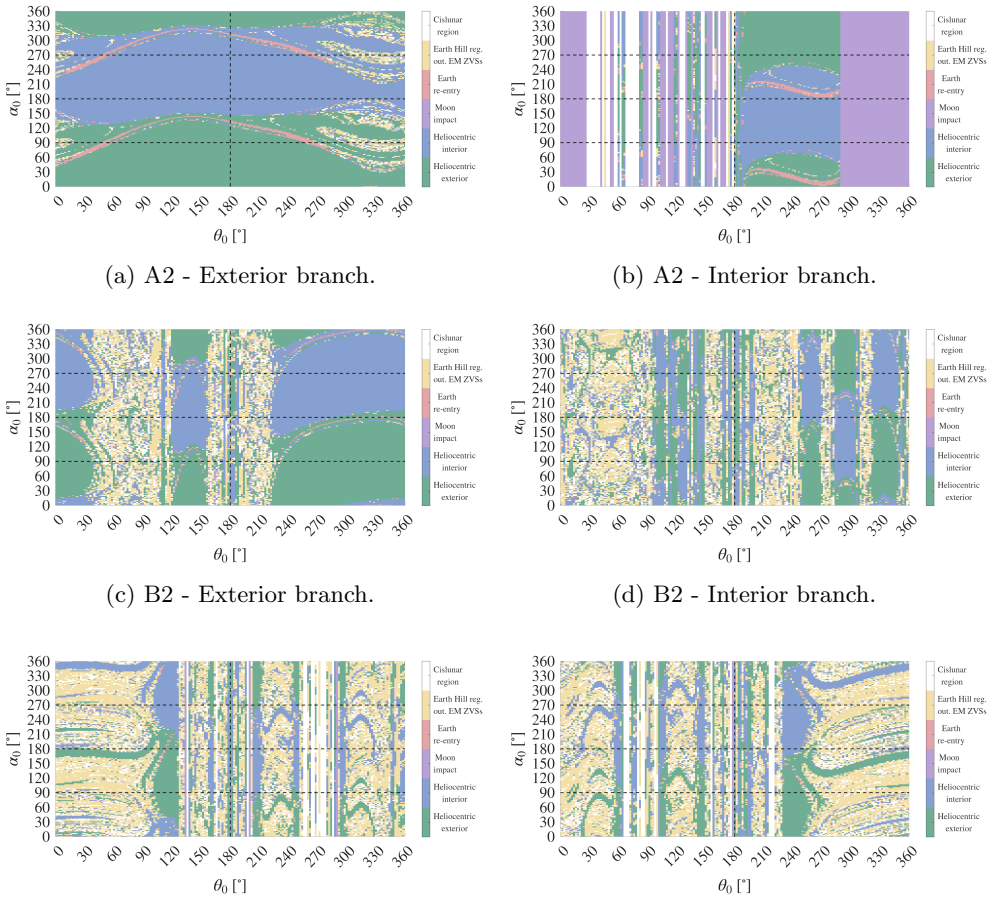

(a) A2 - Exterior branch.

(b) A2 - Interior branch.

(c) B2 - Exterior branch.

(d) B2 - Interior branch.

(e) C2 - First branch.

(f) C2 - Second branch.

Fig. 11: Fate maps obtained from the propagation of the unstable manifolds of the reference LPOs centred at L_2, considering the exterior (right) and interior (left) branches, as a function of θ_0 and α_0. In the maps, blue indicates trajectories reaching the heliocentric exterior region, green indicates trajectories reaching the heliocentric interior region, purple denotes Moon impacts, red denotes Earth re-entries, yellow indicates trajectories whose final state lies in the region within Earth's Hill sphere and outside the EM ZVSs, and white indicates trajectories whose final state lies in the cislunar region.

The behaviour observable in the maps, which reflects the evolution of the unstable manifold of B2, is primarily due to the orbit's high linear stability, which is also related to this latter characteristic. The manifold evolves for a long time in the vicinity of the

LPO before moving away from it, and then shifts mainly towards the outer region of the EM ZVSs, as shown in Fig. 12.

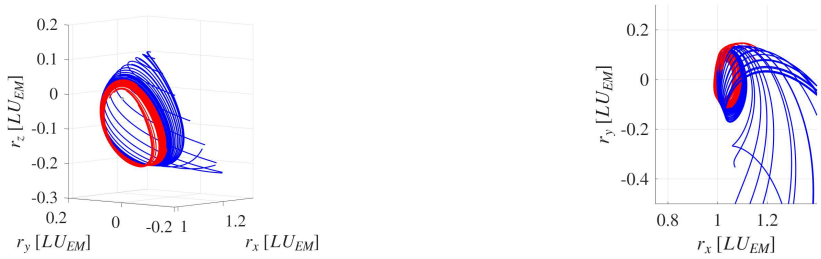

Fig. 12: Exterior (blue) and interior (red) unstable manifold branches departing from B2, when considering a propagation time equal to 45 days (left) and 60 days (right).

In this case, unlike what happens for NRHOs, both the interior and exterior manifold branches exist, as the maximum eigenvalue of the monodromy matrix associated with B2 is positive. However, instead of departing directly from the LPO and moving towards the Moon, the interior branch performs multiple revolutions around B2 before gradually escaping, predominantly toward the EM-L_2 bottleneck. As a result, the interior branch leads to trajectories escaping the Moon's vicinity, with most of them remaining confined in the region within Earth's Hill sphere and outside the EM ZVSs, while only a smaller fraction, compared with the exterior branch, reaches the heliocentric region. The relatively small number of Moon impacts is also related to the large out-of-plane amplitude of B2 and, consequently, of its associated unstable manifold.

The behaviour observed for C2, the reference NRHO in EM-L_2, is the most complex among the cases analysed (see Fig. 11e and Fig. 11f). First, the Möbius strip structure of the unstable manifold is clearly reflected in the fate maps, as a condition encountered at the beginning of the first branch, with $\theta_0 = 0°$, reappears at the end of the second branch, with $\theta_0 = 360°$. In other words, there is continuity between the

beginning of one branch and the end of the other, and vice versa. Moreover, in this particular case, the behaviour associated with the first branch is almost a mirror image of that associated with the second branch. This feature is not common to all NRHOs but is specific to orbit C2 and some others in this subset of the Halo family. The first branch is associated with $\boldsymbol{W^u(0)} = [0.8488; -0.3571; -0.0533; 0.1656; -0.3287; 0.1167]$, while the second branch corresponds to $-\boldsymbol{W^u(0)}$. Overall, the fate maps exhibit a more scattered and less structured behaviour than that observed for orbits A2 and B2.

Fig. 13 shows the fate maps associated with the reference LPOs centred at EM-L_1.

First of all, the behaviours previously described for the evolution of the fate maps of LPOs in EM-L_2 are also found for the LPOs in EM-L_1. Fig. 13b shows the fate map related to the interior unstable manifold branch of A1. Many of the analysed cases lead to a Moon impact before escape from the EM ZVSs occurs, as for a certain value of θ_0 Moon impacts consistently occur in the map for any value of α_0. The high number of Moon impacts is a direct consequence of the geometry of trajectories departing from an LPO in EM-L_1. To escape the EM ZVSs, these trajectories must first pass through the vicinity of the Moon by crossing the yz plane at $x_{EM} = 1 - \mu_{EM}$. This naturally increases the probability of a lunar collision, and the quasi-planar nature of A1 further enhances this effect, leading to an even higher likelihood of Moon impacts. As for A1 exterior manifold branch, with its related results shown in Fig. 13a, it must first pass through the EM-L_1 bottleneck and then transfer towards the Earth's vicinity before eventually reaching the region within Earth's Hill sphere and outside the EM ZVSs. As a consequence, many trajectories do not escape the EM ZVSs within the considered time frame. This is evidenced by the regions of the fate map where cislunar final states are obtained for a given value of θ_0, regardless of the value of α_0.

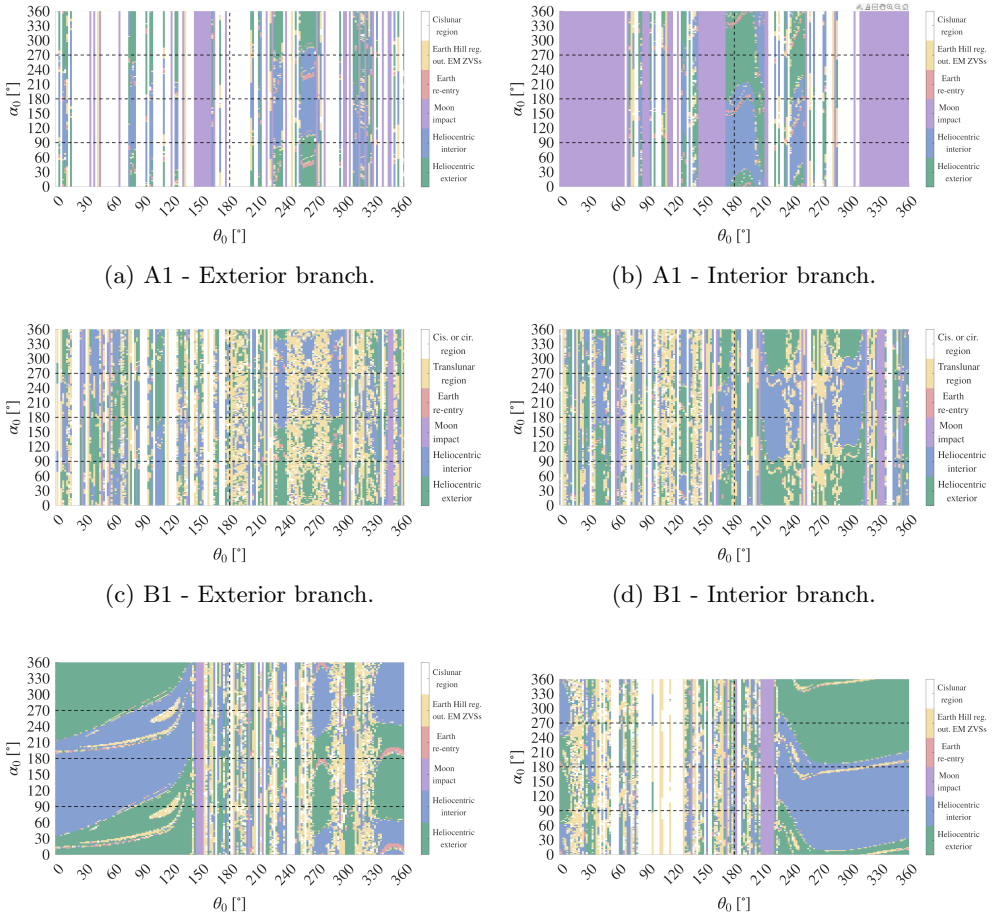

(a) A1 - Exterior branch.

(b) A1 - Interior branch.

(c) B1 - Exterior branch.

(d) B1 - Interior branch.

(e) C1 - First branch.

(f) C1 - Second branch.

Fig. 13: Fate maps obtained from the propagation of the unstable manifolds of the reference LPOs centred at L_1, considering the exterior (right) and interior (left) branches, as a function of θ_0 and α_0. In the maps, blue indicates trajectories reaching the heliocentric exterior region, green indicates trajectories reaching the heliocentric interior region, purple denotes Moon impacts, red denotes Earth re-entries, yellow indicates trajectories whose final state lies in the region within Earth's Hill sphere and outside the EM ZVSs, and white indicates trajectories whose final state lies in the cislunar region.

As for the fate maps associated with orbit B1, they exhibit a behaviour similar to that observed for B2. This is expected, as their unstable manifolds evolve in comparable ways, while both orbits possess similar out-of-plane amplitudes and comparable

linear stability indices.

The fate maps associated with orbit C1, on the other hand, once again display the same Möbius strip-like structure already observed for C2. The direction of the unstable manifold related to C1 first branch is $\boldsymbol{W^u(0)} = [0.4468; -0.7002; -0.0569; 0.0301; -0.4041; -0.3778]$. What is particularly interesting in this case, and differs from the EM-L_2 scenario, is that C1 appears to be the most promising LPO around L_1 when the objective is to reach the heliocentric region. This can be partially attributed to its high out-of-plane amplitude, which reduces the likelihood of Moon impacts, but it is also worth noting that orbital stability appears to be more closely related to the time required for a trajectory to escape a given dynamical regime than to the maximum distance that the trajectory can reach from its initial condition. In other words, a less stable orbit does not necessarily provide access to more distant regions of space; rather, it tends to accelerate the transport process toward them when the initial configuration of the object is favourable.

10 Preliminary analysis of fate map derived trajectory behaviours and their application to end-of-life disposal strategies

A further analysis of some of the trajectories whose outcomes at the end of the propagation are depicted in the fate maps is reported in this Section. Figure 14 summarises a selection of trajectories associated with the behaviours considered the most significant among those observed in the fate map corresponding to the exterior unstable manifold of orbit A2.

At the centre of Fig. 14, two maps are presented. On the left, the reference fate map is shown, surrounded by a selection of representative trajectories of interest, each linked

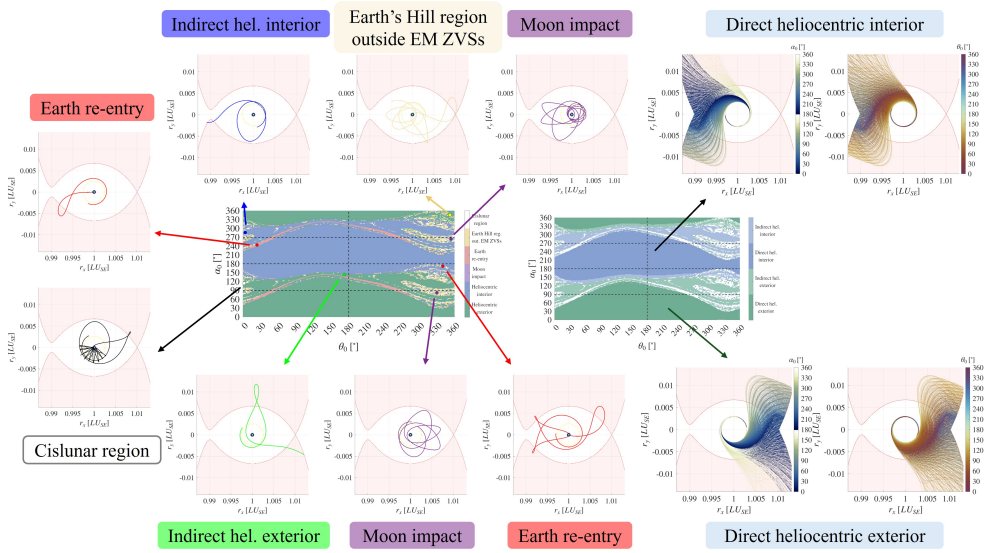

Fig. 14: Summary of selected trajectory characteristics associated with the outcomes represented in the maps, with reference to the exterior unstable manifold branch of A2. Centre left: fate map showing the outcome of unstable manifold trajectory propagation as a function of θ_0 and α_0. Centre right: map highlighting only escape cases, differentiated between direct and indirect escape.

to the corresponding values of θ_0 and α_0 from which it originates. On the right, a second fate map is reported, displaying only the cases associated with reaching heliocentric space and, identified by a darker colour, direct escape options. A direct escape is defined as a trajectory that departs from the reference LPO and reaches the heliocentric region of the system, either exterior or interior, without performing multiple revolutions around any of the system's primaries. These trajectories are of particular interest when considering heliocentric disposal strategies, as they correspond to a rapid escape from the system. The trajectories associated with direct escapes are shown above and below the fate map on the right side of the figure, corresponding respectively to escapes through SE-L_1 and SE-L_2. Their distribution is represented as a function of α_0 and θ_0, clarifying the symmetry between conditions useful for reaching the heliocentric interior or exterior regime. The map associated with direct

escape conditions is also reported on the left of Fig.15, to improve its readability.

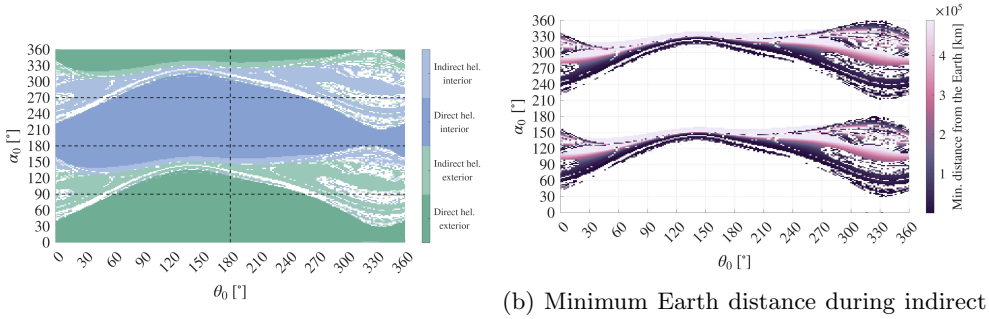

(a) Direct and indirect escapes.

(b) Minimum Earth distance during indirect escape.

Fig. 15: Fate maps obtained from the propagation of the unstable manifolds of the reference LPOs centred at L_2, considering the exterior (right) and interior (left) branches, as a function of θ_0 and α_0. In the maps, blue indicates trajectories reaching the heliocentric exterior region, green indicates trajectories reaching the heliocentric interior region, purple denotes Moon impacts, red denotes Earth re-entries, yellow indicates trajectories whose final state lies in the region within Earth's Hill sphere and outside the EM ZVSs, and white indicates trajectories whose final state lies in the cislunar region.

On the left side of the map, two cases corresponding to trajectories that indirectly reach the interior and exterior heliocentric regions are highlighted in blue and green, respectively. Unlike the direct escape cases, both trajectories perform an additional revolution around the Earth before reaching the heliocentric region. Although they may still be considered as secondary options for heliocentric disposal, their transfer is less direct, slower and therefore generally less appealing.

Two examples of Moon impact trajectories are also reported, identified in purple. Given the considered orbit and manifold direction, these trajectories first escape through the EM-L_2 bottleneck and subsequently re-enter the EM region before eventually impacting the Moon. As such, they are highly chaotic trajectories and resemble resonant-like behaviours within the Sun-Earth-Moon system. Consequently, they are not recommended as disposal strategies. If a lunar impact is the desired objective,

it is preferable to target it by selecting, in this case, the opposite manifold branch. Indeed, the fate map shown in Fig. 11b exhibits extended regions characterised consistently by Moon impacts, regardless of the selected value of α_0. This indicates that the impact occurs before the transition between the EM CR3BP and the SE CR3BP takes place, making these cases more predictable and therefore more suitable as potential disposal options.

Two examples of Earth re-entry trajectories are highlighted in red. These cases represent some of the most interesting dynamical behaviours observed in the analysed set of trajectories. The trajectories leading to Earth re-entry appear to be associated either with resonance phenomena, as is also the case for lunar impacts, with dynamics resembling those of Earth-to-Moon transfers designed using the Weak Stability Boundary (WSB) concept (upper-left panel in the figure), or with a combination of both mechanisms (lower-central panel in the figure). From the perspective of disposal applications, these Earth re-entry trajectories are not ideal candidates, as they are characterised by ToFs of 3-4 months and would likely require significant operational monitoring and control. It would be more practical to consider trajectories enabling a faster and more controlled re-entry, rather than relying solely on the natural trajectory evolution. Nevertheless, these kinds of behaviours are particularly interesting because the dynamical evolution of some of them resembles that of low-energy Earth-to-Moon transfers, but in reverse. This suggests that similar maps could potentially be developed to support the identification of WSB-like trajectories, or that some of the trajectories presented here might even be employed as initial guesses for the design and optimisation of future transfer trajectories. To support this claim, the right-hand side of Fig. 15 shows the minimum Earth distance reached by trajectories undergoing indirect escape. An interesting feature is that this quantity reaches very small values, particularly in the vicinity of the region corresponding to Earth re-entries. This observation is noteworthy for two main reasons. First, it highlights an

underlying continuity in the fate maps that is not immediately apparent. A complete understanding of this continuity would require a dedicated investigation, which lies beyond the scope of the present work. Second, it shows that some trajectories naturally reach regions located at a wide range of altitudes, including distances very close to the Earth, eventual possible candidates for transfer design purposes.
Examples of trajectories whose final states lie in the region within Earth's Hill sphere and outside the EM ZVSs or in the cislunar region are highlighted in yellow and black, respectively. Also in this case, the identified trajectories appear to settle into specific resonant configurations.

In conclusion, two important aspects should be emphasised. First, the behaviours presented here represent only a small subset of those actually identified within the fate maps. They are not all reported for the sake of brevity and because a complete characterisation would require a more comprehensive classification, which is beyond the scope of the present work. Second, although the examples presented here refer specifically to the exterior branch of the unstable manifold associated with orbit A2, similar behaviours are observed across all the analysed cases. The differences among them can be primarily attributed to the initial evolution of the manifold in the vicinity of the reference LPO, as discussed in the previous section, as well as to the corresponding energy levels of the trajectories.

As a final note, the behaviours identified can be related to various EoL strategies; however, it is important to emphasise that demonstrating the existence of operationally feasible disposal options remains a different objective from the one covered in this work and will require analyses different from those presented. Some of the trajectories related to access to different regions of the Sun-Earth-Moon system are associated

with particular disposal strategies solely because refining them could, ultimately, lead to the definition of viable EoL trajectories, not because the two are directly equivalent.

11 Jacobi constant evolution in relationship to the fate maps behaviour

The results presented in Section 8 and 9 suggest that the behaviours observed in the fate maps are primarily driven by three factors: the evolution of the manifold during the initial transient phase in the vicinity of the reference LPO, the degree of hyperbolicity of the manifold trajectories with respect to the Earth, and the effect of the Sun's tidal acceleration once the trajectories enter the SE CR3BP. These three mechanisms can be collectively summarised through the distribution of the JC of the trajectories, shown as a function of α_0 and θ_0 in Fig. 16 with reference to orbits A2 and A1. The JC is evaluated within the SE CR3BP at the instant when the dynamical model first transitions from the EM CR3BP to the SE CR3BP, i.e. when the influence of the Sun on the trajectory becomes greater than that of the Moon. Note that the evaluation of the JC is instantaneous and is performed in the SE system at a specific instant; therefore, its computation is not influenced by any future transitions between the SE and EM systems.

First, it is worth recalling that all the trajectories represented in the previous Figures originate with essentially the same energy level in the EM system. Indeed, the A1 and A2 LPOs have similar JCs as computed in the EM CR3BP, and consequently their associated manifolds also possess comparable energy levels. However, the trajectories reach different energy levels depending on the relative position of the object within the SE system when the influence of the Sun becomes non-negligible. In general, lower values of the JC as evaluated in the SE CR3BP, JC_{SE}, are associated in the fate maps with trajectories that reach the heliocentric region more easily than others. Conversely, higher JC_{SE} values correspond to trajectories characterised by

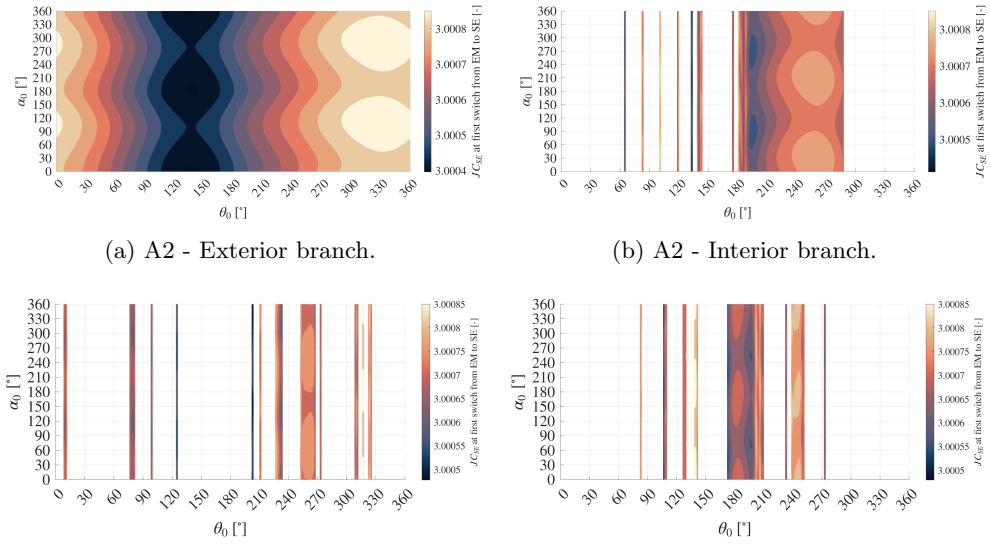

(a) A2 - Exterior branch.

(b) A2 - Interior branch.

(c) B2 - Exterior branch.

(d) B2 - Interior branch.

Fig. 16: Maps illustrating the evolution of the JC computed in the SE CR3BP at the instant when the dynamics first transition from the EM to the SE CR3BP. The corresponding values of JC_{SE} are reported as functions of θ_0 and α_0. The maps in the upper panel are associated with orbit A2, those in the lower panel with A1. When the transition to the SE CR3BP does not happen, the maps are left blank.

a lower degree of hyperbolicity with respect to the Earth, as it can be deduced by comparing Fig.16a with Fig.8. These trajectories exhibit a less predictable dynamical behaviour and possess lower energy levels when inserted in the SE system. The idea that access to the heliocentric region requires the achievement of a sufficiently high energy level had already been introduced, for example, by Boudad et al. (2022). The present results confirm this trend, despite the differences in both the dynamical model and the methodology adopted here. The contraction and expansion of the high-energy regions as α_0 varies are related to the quadrant in which the trajectory transitions from one dynamical model to the other. Furthermore, the isolated structures visible in the maps where not all trajectories enter the domain governed by the SE dynamics are indicative of the strong sensitivity of the system in those areas. In some cases, these structures correspond to isolated trajectories that rapidly reach the

heliocentric region; however, precisely because they are isolated, they are unlikely to represent robust or practically useful disposal solutions.

12 Relationship between Finite Time Lyapunov Exponent evolution and fate maps

Another dynamical indicator whose behaviour is worth investigating in relation to the fate maps is the FTLE, already introduced in Section 2. As discussed therein, its computation depends on a prescribed characteristic time and is associated with a specific dynamical model, which in the present work is either the EM CR3BP or the SE CR3BP. The distribution of the FTLE computed in the SE CR3BP for four different characteristic times, t^*, namely 10, 40, 80, and 120 days, and referring to the exterior and interior branches of the unstable manifold of orbit A2, is shown in Fig. 17. The characteristic time is measured starting from the instant at which a trajectory first transitions from the EM CR3BP to the SE CR3BP, as adopted for the evaluation of JC_{SE} in the previous Section. Consequently, this transition instant is taken as the initial time ($t^* = 0$) for the FTLE computation. Note that, in this case as well, the FTLE computation is based solely on the SE CR3BP, and no additional transitions to the EM system are considered. The state transition matrices from which the FTLE values are derived are computed from the propagation of a state in the SE system only, taking the state at the first transition from the EM to the SE CR3BP as the initial condition ($t^* = 0$).

The first aspect that can be observed is that, at early characteristic times, the relationship between the FTLE maps and the corresponding fate maps appears to be partial, but as t^* increases, the connection becomes progressively clearer, and the FTLE maps gradually develop a structure that closely resembles the corresponding fate maps. Considering the FTLE maps computed with a characteristic time of 10 days, the trajectories associated, for example, with direct escape appear to correspond to the lowest

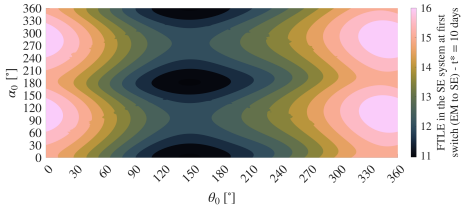

(a) A2 - Exterior branch, $t^* = 10$ days

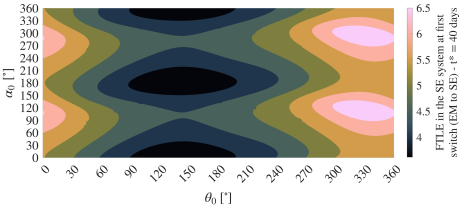

(b) A2 - Exterior branch, $t^* = 40$ days

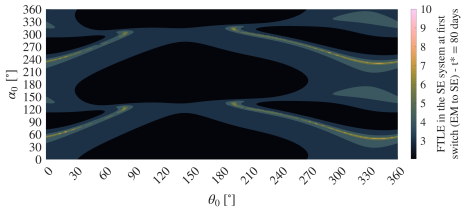

(c) A2 - Exterior branch, $t^* = 80$ days

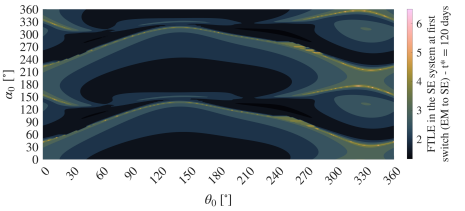

(d) A2 - Exterior branch, $t^* = 120$ days

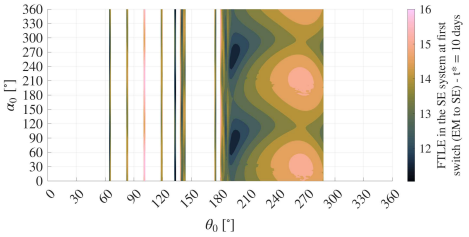

(e) A2 - Interior branch, $t^* = 10$ days

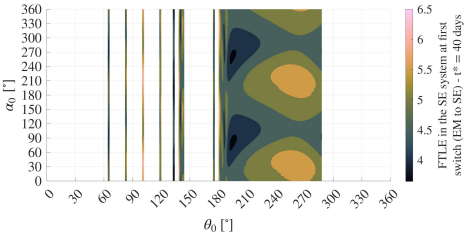

(f) A2 - Interior branch, $t^* = 40$ days

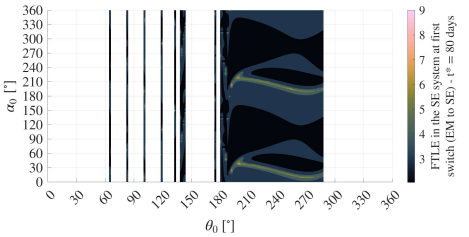

(g) A2 - Interior branch, $t^* = 80$ days

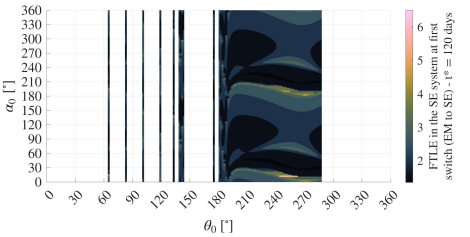

(h) A2 - Interior branch, $t^* = 120$ days

Fig. 17: FTLE maps obtained from the propagation of the exterior and interior branches of the unstable manifold of orbit A2 for different characteristic times, t^*. The characteristic time is measured from the instant of the first transition from the EM CR3BP to the SE CR3BP, which corresponds to $t^* = 0$.

FTLE values (relative to the scale associated with the considered characteristic time

rather than in an absolute sense). These low values indicate a reduced sensitivity of the trajectory outcome to perturbations of the initial conditions or, in other words, small perturbations are less likely to alter the final state reached by the trajectory. Conversely, trajectories exhibiting a low degree of hyperbolicity with respect to the Earth are associated with the highest FTLE values, which indicates a stronger sensitivity to perturbations. This behaviour is consistent with the patterns observed in the corresponding fate maps.

When considering the FTLE maps obtained with a characteristic time of 120 days, this relationship becomes even more evident. High FTLE values are observed, for instance, in regions associated with Earth-return trajectories resembling WSB transfers, as well as in regions corresponding to resonant-like trajectories. This result is consistent with the interpretation of FTLE ridges as expressions of underlying dynamical structures, such as Lagrangian coherent structures, as previously discussed. The results related to both the exterior and interior unstable manifold branches of A1 are reported in Fig.18 The results obtained for orbit A1 confirm the observations previously discussed for A2. Of particular interest, with regard to the FTLE, is the fact that this indicator can be applied to any dynamical system, whether autonomous or non-autonomous, and its definition is not restricted to the CR3BP, unlike, for instance, the JC. This suggests that the FTLE could serve as a bridge between the simplified dynamical models employed in this work and more realistic representations of the dynamical environment, such as ephemeris-based models, facilitating the transfer of results obtained from approximated models to higher-fidelity dynamical frameworks. Consequently, the investigation of FTLE-based analyses within more realistic models represents a particularly promising direction of future work.

The results obtained for other orbits are qualitatively similar to those presented here and are therefore omitted for the sake of brevity.

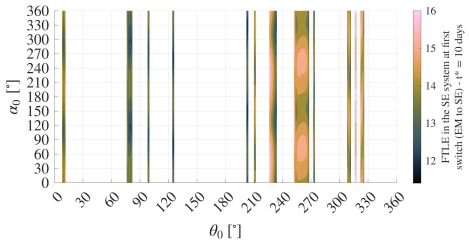

(a) A1 - Exterior branch, $t^* = 10$ days

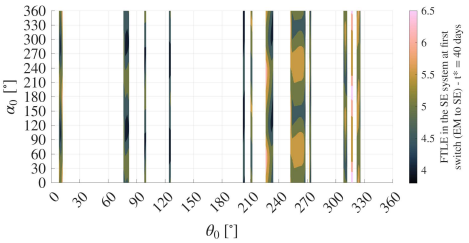

(b) A1 - Exterior branch, $t^* = 40$ days

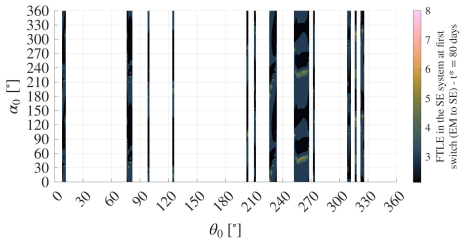

(c) A1 - Exterior branch, $t^* = 80$ days

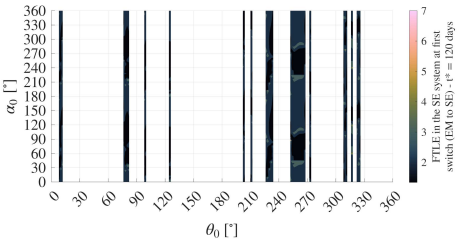

(d) A1 - Exterior branch, $t^* = 120$ days

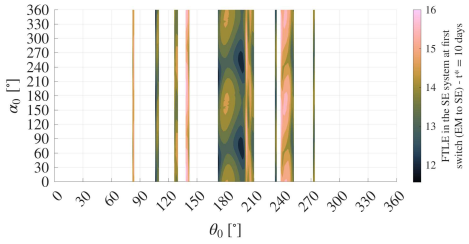

(e) A1 - Interior branch, $t^* = 10$ days

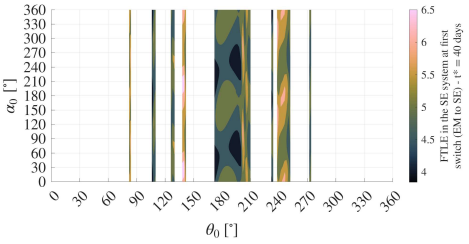

(f) A1 - Interior branch, $t^* = 40$ days

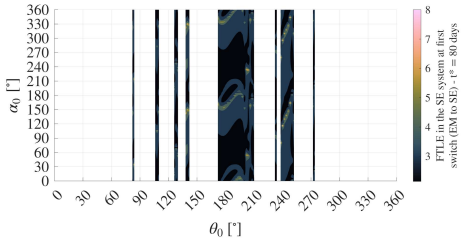

(g) A1 - Interior branch, $t^* = 80$ days

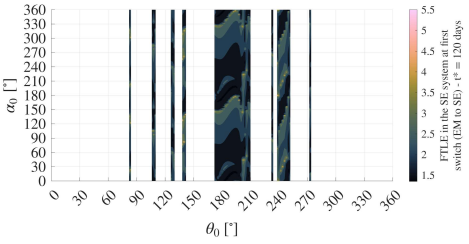

(h) A1 - Interior branch, $t^* = 120$ days

Fig. 18: FTLE maps obtained from the propagation of the exterior and interior branches of the unstable manifold of orbit A1 for different characteristic times, t^*. The characteristic time is measured from the instant of the first transition from the EM CR3BP to the SE CR3BP, which corresponds to $t^* = 0$.

13 Conclusions and future works

The region of space extending from highly eccentric geostationary orbits to the EM Lagrange points currently represents one of the most promising areas for future space missions. If the schedules of major space agencies and private companies develop as expected, this region will experience a significant increase in traffic over the coming years. Such growth may eventually lead to space traffic management challenges arising from the progressive congestion of this environment, similar to those already observed in near-Earth orbits.

To prevent a problem that could become even more difficult to manage than the current space debris issue in the Earth neighbourhood, it is essential to begin developing mitigation strategies early on. In other words, rather than addressing the consequences of an increasingly crowded EM environment, efforts should focus first on preventing the generation of debris. One of the most effective approaches is to investigate low-cost transport pathways originating from orbital configurations considered promising operational candidates, such as LPOs, as a deeper understanding of these transport mechanisms can support the design of EoL disposal strategies capable of accommodating a wide range of mission scenarios and operational requirements.

In this work, these pathways have been investigated by considering six LPOs as reference cases: two Halo orbits and one NRHO around EM-L_2, together with their corresponding counterparts around EM-L_1. Their unstable manifolds have been propagated within the framework of the coupled EM and SE CR3BP, considering a maximum propagation time of 12 months. This process led to the generation of fate maps, each associated with a branch of the unstable manifold of a given LPO. These maps describe the final state reached by the trajectory as a function of two initial conditions: θ_0, the phase angle along the reference LPO, and α_0, the relative phase angle between the EM and SE systems at the departure from the reference LPO.

The main conclusions that can be drawn from the analysis of the fate maps are as follows:

1. The outcomes observed in the fate maps are strongly influenced by the initial behaviour of the manifold while it remains in the vicinity of the reference orbit, as well as by the timescale over which the trajectory departs from it. This behaviour is primarily governed by the stability properties and geometric characteristics of the LPO itself.
2. The reason why, given a fixed initial perturbation, certain values of θ_0 are associated with trajectories that reach the heliocentric region more readily than others can be traced back to their degree of hyperbolicity with respect to the Earth.
3. Once the trajectory reaches a region of space where the influence of the Sun can no longer be neglected, its position within the SE system, combined with the factors described above, plays a key role in determining its subsequent evolution and the regions of space it may reach.

A comparison among the different LPOs considered in this study was also performed, together with a preliminary assessment of the potential relationship between the various outcomes identified in the fate maps and possible EoL disposal strategies. The main conclusion that can be drawn in this regard is that, as a general rule, highly unstable orbits should be preferred from an EoL disposal perspective. More specifically, orbits located in the vicinity of either of the two libration points generally represent the most favourable candidates, depending on the disposal strategy to be evaluated. NRHOs also appear to be viable candidates, although their dynamical characteristics clearly make their exploitation more challenging. Conversely, orbits characterised by high levels of linear stability, particularly those located near bifurcation points of the Halo family, should generally be avoided. From this perspective, a promising future work path would be the identification of heteroclinic connections linking a given LPO to another periodic orbit that may be better suited to the desired disposal strategy,

thereby enabling the design of more effective EoL trajectories. It has also been shown that the evolution of both the JC_{SE} and the FTLE, when evaluated at selected stages of trajectories' evolution, provides valuable insight into and physical reasons for the distribution of final states observed in the fate maps. The quantity JC_{SE}, when evaluated at the first transition from the EM to the SE system, is low for solutions which are highly hyperbolic with respect to the Earth early on, i.e., solutions related to direct escape. The evolution of the FTLE in the SE CR3BP is shown as a function of the characteristic time, considered equal to zero at the first transition between the EM and SE systems. As the characteristic time increases, the patterns observed in the fate maps can be identified in the FTLE maps too, with low FTLE values corresponding to regions characterised by regular behaviour and higher FTLE values corresponding to regions characterised by irregular patterns or trajectories exhibiting WSB-like behaviours.

As a first step for future work, a more comprehensive assessment of the relationship between the identified outcomes and current EoL disposal strategies should be performed, with the objective of better highlighting how the findings of this study may be exploited in that context. In addition, the analyses presented here could be extended both to a larger set of LPOs and to higher fidelity dynamical models, including ephemeris-based formulations, to assess the robustness and applicability of the results under more realistic conditions.

Acknowledgments

This research received funding from the European Research Council (ERC) under the European Union's Horizon Europe research and innovation program as part of the GREEN SPECIES project (Grant agreement No - 101089265), and as part of the work developed for the agreement n. 2023-37-HH.0 for the project "Attività tecnico-scientifiche di supporto a C-SSA/ISOC e simulazione di architetture di sensori per

SST", established between ASI, Italian Space Agency, and POLIMI, Politecnico di Milano. The authors would also like to acknowledge Crameri (2023), to whom credit is due for the colour maps used throughout this work.

Availability of data and materials

Data sets generated during the current study are available from the corresponding author upon reasonable request. The ephemeris data relative to the various celestial bodies considered were obtained from NASA's SPICE toolkit: NASA SPICE (2025)

Declaration of interests

The authors have no competing interests to declare that are relevant to the content of this article.

References

Alessi EM (2015) The reentry to Earth as a valuable option at the end-of-life of Libration Point Orbit missions. Advances in Space Research 55(12):2914–2930. https://doi.org/10.1016/j.asr.2015.03.012

Alessi EM, Gómez G, Masdemont JJ (2009) Leaving the Moon by means of invariant manifolds of libration point orbits. Communications in Nonlinear Science and Numerical Simulation 14(12):4153–4167. https://doi.org/10.1016/j.cnsns.2008.09.016

Alessi EM, Gómez G, Masdemont JJ (2010) Two-manoeuvres transfers between LEOs and Lissajous orbits in the Earth–Moon system. Advances in Space Research 45(10):1276–1291. https://doi.org/10.1016/j.asr.2009.12.010

928 Anderson RL, Lo MW, Born GH (2003) Application of local lyapunov exponents
929 to maneuver design and navigation in the three-body problem. In: AAS/AIAA
930 Astrodynamics Specialist Conference, Big Sky, Montana, USA

931 Andrievskaia D, Cáceres I, Guardabasso P, et al (2022) Analysis of lunar impacts
932 for orbital debris mitigation. In: 73rd International Astronautical Congress, Paris,
933 France

934 Armellin R, Rasotto M, Di Lizia P, et al (2015) End-of-life disposal of libration point
935 orbit missions: The case of GAIA. Advances in Space Research 56(3):461–478. https:
936 //doi.org/10.1016/j.asr.2015.03.014

937 Baker-McEvilly B, Bhadauria S, Canales D, et al (2024) A comprehensive review on
938 cislunar expansion and space domain awareness. Progress in Aerospace Sciences
939 147:101019. https://doi.org/10.1016/j.paerosci.2024.101019

940 Belbruno EA, Miller JK (1993) Sun-perturbed Earth-to-Moon transfers with ballistic
941 capture. Journal of Guidance, Control, and Dynamics 16(4):770–775. https://doi.
942 org/10.2514/3.21079

943 Black A, Frueh C (2025) Fragmentation characterization in the circular restricted three
944 body problem for cislunar space domain awareness. Advances in Space Research
945 75(1):1177–1204. https://doi.org/10.1016/j.asr.2024.08.076

946 Bolis M, Alessi EM, Colombo C (2026a) A comparative assessment of heliocentric and
947 controlled lunar impact end-of-life disposal strategies for near rectilinear halo orbits.
948 Acta Astronautica 247:743–764. https://doi.org/10.1016/j.actaastro.2026.05.039

949 Bolis M, Alessi EM, Colombo C (2026b) No-return disposal trajectories in the Earth-
950 Moon system: A parametric analysis. Aerospace Science and Technology 178:112452.
951 https://doi.org/10.1016/j.ast.2026.112452

Bolis M, Alessi EM, Sánchez Cuartielles JP, et al (2026c) Cislunar end-of-life strategies based on an aware usage of key dynamical objects. In: 30th International Symposium on Space Flight Dynamics, Toulouse, France, 2026

Boone NR, Bettinger RA (2025) Efficient disposal of low lunar orbiters on the lunar surface. Journal of Space Safety Engineering 12(1):195–205. https://doi.org/10.1016/j.jsse.2024.09.005

Boone NR, Bettinger RA, Little BD (2025) Simulation of Debris Events in Cislunar Orbits Near the Moon. Journal of Spacecraft and Rockets 62(6):2030–2046. https://doi.org/10.2514/1.A36072

Boudad KK, Howell KC, Davis DC (2022) Departure and Escape Dynamics from the Near Rectilinear Halo Orbits in the Earth-Moon-Sun System. The Journal of the Astronautical Sciences 69:1076 – 1114. https://doi.org/10.1007/s40295-022-00328-w

Bucchioni G, De Benedetti M, D'Onofrio F, et al (2022) Fully safe rendezvous strategy in cis-lunar space: Passive and active collision avoidance. The Journal of the Astronautical Sciences 69:1319 – 1346. https://doi.org/10.1007/s40295-022-00339-7

Bucci L, Kleinschneider A, Lavagna M, et al (2018) Optimal escape manifolds for cislunar halo orbits. In: 69th International Astronautical Congress (IAC), Bremen, Germany

Canales D, Howell K (2024) Understanding flow around planetary moons via finite-time Lyapunov exponent maps. Celestial Mechanics and Dynamical Astronomy 136. https://doi.org/10.1007/s10569-024-10213-3

974 Carton L, Rosengren AJ (2025) End-of-life cislunar disposal orbits: Evaluating the
975 effectiveness and sustainability of lunar impacts. In: 76th International Astronauti-
976 cal Congress, Sydney, AUstralia

977 Castelli R (2011) On the Relation Between the Bicircular Model and the Cou-
978 pled Circular Restricted Three-Body Problem Approximation, Springer New York,
979 chap 1

980 Celletti A (2010) Stability and Chaos in Celestial Mechanics. Springer Berlin,
981 Heidelberg, https://doi.org/10.1007/978-3-540-85146-2

982 Colombo C, Alessi EM, Van der Weg W, et al (2015) End-of-life disposal concepts
983 for Libration Point Orbit and Highly Elliptical Orbit missions. Acta Astronautica
984 110:298–312. https://doi.org/10.1016/j.actaastro.2014.11.002

985 Crameri F (2023) Scientific colour maps. zenodo. https://doi.org/10.5281/zenodo.
986 1243862

987 Davis DC (2011) Multi-body trajectory design strategies based on periapsis poincaré
988 maps. PhD thesis, Purdue University, West Lafayette, Indiana

989 Davis DC, Boudad KK, Phillips SM, et al (2019a) Disposal, deployment, and debris
990 in near rectilinear halo orbits. In: AAS/AIAA Space Flight Mechanics Meeting,
991 Ka'anapali, Maui, Hawaii, USA

992 Davis DC, Boudad KK, Power RJ, et al (2019b) Heliocentric escape and lunar
993 impact from near rectilinear halo orbits. In: AAS/AIAA Astrodynamics Specialist
994 Conference, Portland, Maine, USA

995 Doedel EJ, Romanov VA, Paffenroth RC, et al (2007) Elemental periodic orbits
996 associated with the libration points in the circular restricted 3-body problem. Inter-
997 national Journal of Bifurcation and Chaos 17(08):2625–2677. https://doi.org/10.
998 1142/S0218127407018671

999 ESA Space Debris Mitigation Working Group (2023) Esa space debris mitigation
1000 requirements. Tech. rep., ESA

1001 European Space Policy Institute (ESPI) (2025) Espi report 96 - towards a safe
1002 and sustainable cislunar space: Policy priorities for european engagement - full
1003 report. Tech. rep., available at: https://www.espi.eu/wp-content/uploads/2025/07/
1004 ESPI-Report-96_Cislunar-Safety.pdf

1005 Frueh C, Howell K, DeMars KJ, et al (2021) Cislunar space situational awareness. In:
1006 31st AIAA/AAS Space Flight Mechanics Meeting, virtual

1007 Gambarotto C, Grattagliano P, De Maria L, et al (2026) Monitoring cislunar frag-
1008 mentation events using a constellation of space-based observers. Acta Astronautica
1009 238:1432–1446. https://doi.org/10.1016/j.actaastro.2025.09.078

1010 García F, Gómez G (2007) A note on weak stability boundaries. Celestial Mechanics
1011 and Dynamical Astronomy 97:87–100. https://doi.org/10.1007/s10569-006-9053-6

1012 Guardabasso P (2023) Study of cislunar dynamics and environment for the man-
1013 agement of space debris. PhD thesis, Institut Supérieur de l'Aéronautique et de
1014 l'Espace

1015 Guardabasso P, Skoulidou DK, Bucci L, et al (2023) Analysis of accidental spacecraft
1016 break-up events in cislunar space. Advances in Space Research 72(5):1550–1569.
1017 https://doi.org/10.1016/j.asr.2023.05.004

Gómez G, Llibre J, Martínez R, et al (2001) Station keeping of libration point orbits. ESOC contract 5648/83/D/JS(SC), final report, European Space Agency, 1985. Reprinted as: *Dynamics and Mission Design Near Libration Points Vol.1 Fundamentals: The Case of Collinear Libration Points*. World Scientific Monograph Series in Mathematics

Howell K (1984) Three-dimensional, periodic "halo" orbits. Celestial mechanics 32(1):53–71. https://doi.org/10.1007/BF01358403

Àngel Jorba, Nicolás B (2020) Transport and invariant manifolds near L3 in the Earth-Moon Bicircular model. Communications in Nonlinear Science and Numerical Simulation 89:105327. https://doi.org/10.1016/j.cnsns.2020.105327

Koon WS, Lo MW, Marsden JE, et al (2001) Low Energy Transfer to the Moon. Celestial Mechanics and Dynamical Astronomy 81:63–73. https://doi.org/10.1023/A:1013359120468

Koon WS, Lo MW, Marsden JE, et al (2011) Dynamical Systems, the Three-Body Problem and Space Mission Design. Marsden Books

Liu X, Fu S, Wu D, et al (2026) Search strategy for lunar gravity assist escape trajectories based on dynamical analysis in the three-body problem. Aerospace Science and Technology 177:112274. https://doi.org/10.1016/j.ast.2026.112274

Mingotti G, Topputo F, Bernelli-Zazzera F (2009) Low-energy, low-thrust transfers to the Moon. Celestial Mechanics and Dynamical Astronomy 105:61–74. https://doi.org/10.1007/s10569-009-9220-7

NASA SPICE (2025) Available at: https://naif.jpl.nasa.gov/naif/aboutspice.html. Last accessed: 12-02-2026

Nicolás Ávila B (2022) Invariant manifolds and transport in a Sun-perturbed Earth-Moon system. PhD thesis, Department of Mathematics and Computer Science, University of Barcelona, available at: https://hdl.handle.net/2445/190643

Nugent L, Howell K, Davis D (2025) Flexible maneuver planning for collision avoidance in l1/l2 libration point orbits. In: AAS/AIAA Space Flight Mechanics Meeting, Kaua'i, Hawaii, USA

Olikara ZP, Gómez G, Masdemont JJ (2015) Dynamic Mechanisms for Spacecraft Disposal from Sun–Earth Libration Points. Journal of Guidance, Control, and Dynamics 38(10):1976–1989. https://doi.org/10.2514/1.G000581

Oseledets VI (1968) A Multiplicative Ergodic Theorem. Lyapunov Characteristic Numbers for Dynamical Systems. Transactions of the Moscow Mathematical Society 19:197–231

Osinga H (2000) Non-orientable manifolds of periodic orbits, pp 922–924. https://doi.org/10.1142/9789812792617_0180

Osinga HM (2003) Nonorientable manifolds in three-dimensional vector fields. International Journal of Bifurcation and Chaos 13(03):553–570. https://doi.org/10.1142/S0218127403006777

Parker JS, Anderson RL (2014) Low-energy lunar trajectory design. John Wiley & Sons

Parker TS, Chua LO (1989) Practical Numerical Algorithms for Chaotic Systems. Springer New York, NY, https://doi.org/10.1007/978-1-4612-3486-9

Pasquale A, Lavagna M, Renk F (2024) Systematic analysis of cislunar escape opportunities for exploration and planetary defence missions. In: 75th International

Astronautical Congress (IAC), Milan, Italy

Renk F, Hechler M, Messerschmid E (2010) Exploration missions in the Sun–Earth–Moon system: A detailed view on selected transfer problems. Acta Astronautica 67(1):82–96. https://doi.org/10.1016/j.actaastro.2009.10.023

Richmond JHL, Howell KC (2026) Cislunar-to-Deep-Space Transfer Design: Identifying Advantageous CR3BP Departure Orbit Families. In: ASCEND, Washington D.C., USA, https://doi.org/10.2514/6.2026-3114

Sargent RM, Bettinger RA, Hartsfield CR (2025) Preliminary investigation of cislunar disposal reachability via electric propulsion for selected L2 lagrange point orbit families. Discover Space 129. https://doi.org/10.1007/s11038-025-09573-z

Scheuerle ST, Davis DC, Zimovan-Spreen EM, et al (2023) Jettison and disposal from near rectilinear halo orbits, part 1: Theory. In: AAS/AIAA Astrodynamics Specialist Conference, Big Sky, Montana, USA

Scheuerle ST, Howell KC, Davis DC (2025) Energy-informed pathways: A fundamental approach to designing ballistic lunar transfers. Advances in Space Research 75(1):1096–1117. https://doi.org/10.1016/j.asr.2024.07.035

Shimane Y, Tomita K, Ho K (2025) Cislunar space situational awareness constellation design and planning with facility location problem. Journal of Spacecraft and Rockets 62(6):1938–1960. https://doi.org/10.2514/1.A36361

Short CR (2016) Flow-informed strategies for trajectory design and analysis. PhD thesis, Purdue university

Soldini S, Colombo C, Walker S (2016) The end-of-life disposal of satellites in libration-point orbits using solar radiation pressure. Advances in Space Research 57(8):1664–1679. https://doi.org/10.1016/j.asr.2015.06.033

Szebehely V (1967) Theory of Orbit: The restricted problem of three Bodies, 1st edn. Academic Press, https://doi.org/10.1016/B978-0-12-395732-0.X5001-6

Tu F, Wang W, Wu S, et al (2025) Optimal control for low-thrust collision avoidance in CRTBP. Aerospace Science and Technology 167:110643. https://doi.org/10.1016/j.ast.2025.110643

Van der Weg WJ, Vasile M (2014) Sun–Earth L1 and L2 to Moon transfers exploiting natural dynamics. Celestial Mechanics and Dynamical Astronomy 120:287–308. https://doi.org/10.1007/s10569-014-9581-4

Williams DAP (2024) Dynamics of long-term orbit maintenance strategies in the circular restricted three body problem. Master's thesis, School of Aeronautics and Astronautics, Purdue University. Advisor: Prof. Kathleen Howell

Zhang J, Fantino E, Du C, et al (2025) Optimal transfers from an Earth-Moon unstable libration point orbit to the lunar surface. Advances in Space Research 76(6):3528–3547. https://doi.org/10.1016/j.asr.2025.06.072

Zimovan-Spreen EM, Howell KC, Davis DC (2020) Near rectilinear halo orbits and nearby higher-period dynamical structures: orbital stability and resonance properties. Celestial Mechanics and Dynamical Astronomy 132:28. https://doi.org/https://doi.org/10.1007/s10569-020-09968-2